Article

From Discrete to Continuum Models of Three-Dimensional Deformations in Epithelial Sheets

Nebojsa Murisic,[1] Vincent Hakim,[2] Ioannis G. Kevrekidis,[3] Stanislav Y. Shvartsman,[1] and Basile Audoly[4,*]
[1]Lewis-Sigler Institute for Integrative Genomics, Princeton University, Princeton, New Jersey; [2]CNRS & Laboratoire de Physique Statistique, Ecole Normale Supérieure, Paris, France; [3]Chemical and Biological Engineering, Princeton University, Princeton, New Jersey; and [4]Sorbonne Universités, UPMC Univ Paris 06, CNRS, UMR 7190 Institut Jean Le Rond d'Alembert, Paris, France

ABSTRACT Epithelial tissue, in which cells adhere tightly to each other and to the underlying substrate, is one of the four major tissue types in adult organisms. In embryos, epithelial sheets serve as versatile substrates during the formation of developing organs. Some aspects of epithelial morphogenesis can be adequately described using vertex models, in which the two-dimensional arrangement of epithelial cells is approximated by a polygonal lattice with an energy that has contributions reflecting the properties of individual cells and their interactions. Previous studies with such models have largely focused on dynamics confined to two spatial dimensions and analyzed them numerically. We show how these models can be extended to account for three-dimensional deformations and studied analytically. Starting from the extended model, we derive a continuum plate description of cell sheets, in which the effective tissue properties, such as bending rigidity, are related explicitly to the parameters of the vertex model. To derive the continuum plate model, we duly take into account a microscopic shift between the two sublattices of the hexagonal network, which has been ignored in previous work. As an application of the continuum model, we analyze tissue buckling by a line tension applied along a circular contour, a simplified set-up relevant to several situations in the developmental contexts. The buckling thresholds predicted by the continuum description are in good agreement with the results of stability calculations based on the vertex model. Our results establish a direct connection between discrete and continuum descriptions of cell sheets and can be used to probe a wide range of morphogenetic processes in epithelial tissues.

INTRODUCTION

The emergence of epithelial tissues, in which polarized cells adhering to each other and to the extracellular matrix are arranged in continuous sheets, was one of the key steps in the evolution of multicellular animals. In adult organisms, epithelia line the internal surfaces of organs, maintaining their integrity and mediating interactions between different compartments. During embryonic development, epithelia serve as the starting point in the morphogenesis of tissues and organs (1). Epithelial morphogenesis can be accompanied by changes in cell numbers, because of cell division and death. At the same time, early steps in a number of important and well-studied morphogenetic events, including early stages of gastrulation (2), happen at constant cell numbers and do not involve changes in cell connectivity. This is the class of processes considered in this article, in which we aim to develop a coarse-grained description of three-dimensional (3D) tissue deformations, starting from cell-level description of an epithelium.

Recent studies of epithelial morphogenesis (3–7) provide highly resolved kinematic descriptions that set the stage for the development and analysis of mathematical models that can explain and predict the observed cell and tissue deformations. Some of the simplest proposed mathematical descriptions are the so-called vertex models, see (3,8–14), in which the degrees of freedom are the coordinates of the vertices of cells, modeled as planar polygons. The energy of such a model epithelium is evaluated from contributions of terms that account for properties of individual cells, like the preference for a target area value and their tendency to minimize perimeter length because of cortical tension. It also includes cell pairwise interactions, modeled as terms depending on the length of cell-cell edges, as in e.g., (3). Of course, tissue morphogenesis is quite varied, and a number of phenomena, such as cell motion, have been described by models different from vertex models, see (15) for a review. Vertex models have been used to explain the statistics of cell shapes and compartment boundaries in developing epithelia and provide a clear connection between experimental data and simple physical theories (3,12,16,17). In this study, we use the existing models as a starting point for describing out-of-plane deformations of epithelial sheets.

Our results can be summarized as follows. First, we show that a 3D extension of vertex models requires some care in the definition of cell area, which is straightforward when cells are planar, but must be redefined when vertices can move in three dimensions. To properly describe 3D deformations, we also introduce a cell-based description of bending stresses. Second, we use a homogenization approach to derive an effective continuum description of an epithelium, valid on length

Submitted November 14, 2014, and accepted for publication May 13, 2015.
*Correspondence: audoly@lmm.jussieu.fr
Editor: Ruth Baker.

0006-3495/15/07/0154/10 $2.00
http://dx.doi.org/10.1016/j.bpj.2015.05.019

scales larger than a single cell. We resolve the difficulties pointed out in previous studies by properly taking into account the non-Bravais character of the hexagonal lattice. Motivated by a number of experimental studies, e.g., (17), we use the homogenized model to describe epithelial buckling induced by heterogeneities of cell properties. Linear stability analysis of the homogenized problem is in quantitative agreement with the results of direct bifurcation analyses of the extended vertex model that resolves individual cells, suggesting that our approach can describe a wide range of phenomena in developing epithelia.

MATERIALS AND METHODS

The nonplanar vertex model

Originally developed to study foams (18), vertex-based geometrical models have been employed to describe cell sheets since the early work of Honda (8,9). In this approach (3,4,11–13,16), interfaces between cells are defined as straight segments and each cell assumes a polygonal shape. Cell dynamics is described in a simplified way in terms of the motion of the polygon vertices.

Based on these previous works, we introduce a vertex model to describe nonplanar configurations of epithelial cell sheets. We consider a smooth surface endowed with a mesh, as described schematically in Fig. 1. More precisely, the lattice is specified by the positions $\mathbf{x}_v$ of its vertices, where v is a vertex index. The length L_e of an edge labeled by e is $L_e = \left|\mathbf{x}_{v_2(e)} - \mathbf{x}_{v_1(e)}\right|$, where $v_1(e)$ and $v_2(e)$ denote the indices of the vertices at the endpoints of the edge e. The perimeter P_f of a face f is simply the sum of the lengths of its edges e, $P_f = \sum_{e\in f} L_e$.

Next, the energy of a nonplanar configuration of cells is defined by the following:

$$\mathcal{E}_{\mathrm{vm}} = \frac{1}{2}\sum_f \left(A_f - 1\right)^2 + G\sum_e L_e + \frac{H}{2}\sum_f P_f^2 + B\sum_{e'}\left(1 - \mathbf{N}_{f_1(e')}\cdot\mathbf{N}_{f_2(e')}\right). \quad (1)$$

The first and third term run over all faces f, the second term over all edges e, and the last term runs over interior edges e', i.e., edges belonging to two adjacent faces $f_1(e')$ and $f_2(e')$. The quantities G, H, and B are elasticity parameters. The first term (area elasticity) penalizes any deviation from the natural area $A^0 = 1$. For simplicity, we work in a set of units such that both the target area A^0 and the corresponding modulus have the value 1. The second term captures the adhesion energy between cells, when $G<0$. The coefficient G has units of energy per unit length, or force. The third term represents cortical tension (perimeter elasticity). The last term is a bending term to which we will return below. A simpler description is often used with $H = 0$ and $G>0$, which then represents an effective line tension. In the following, we provide analytical results for the general case $G\neq 0, H\neq 0$ and focus on the case $H = 0$ in our simulations.

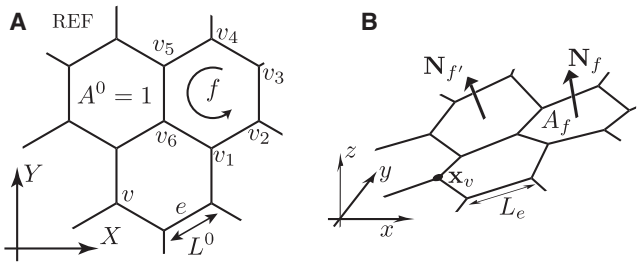

FIGURE 1 The 3D vertex model. (*A*) Schematic drawing of the hexagonal vertex model, showing the vertices, edges, and cell faces in reference configuration. (*B*) Deformation of the reference regular hexagonal configuration into a nonplanar configuration, and unit outward normal vectors.

For planar configurations of the vertices, the bending term vanishes and the energy defined by Eq. 1 coincides with the classical, planar vertex model (3,13). For nonplanar configurations, the area A_f and the unit normal $\mathbf{N}_f$ to a face f appearing in Eq. 1 can be defined in different ways (19) that are all equivalent in the continuous limit. We use the following definitions, which differ slightly from those used in (17) and are more convenient. Let n be the number of vertices of the face f ($n = 6$ for a hexagonal mesh), and $(v_1(f), \ldots, v_n(f))$ be the list of vertices ordered in the counter-clockwise direction, as in Fig. 1. We first define the vector area $\mathbf{A}_f$ of the face f by

$$\mathbf{A}_f = \frac{1}{2}\left(\mathbf{x}_{v_1(f)} \times \mathbf{x}_{v_2(f)} + \mathbf{x}_{v_2(f)} \times \mathbf{x}_{v_3(f)} + \cdots + \mathbf{x}_{v_n(f)} \times \mathbf{x}_{v_1(f)}\right), \quad (2)$$

this quantity being invariant under rigid-body translations of the lattice. Next, we define the scalar area A_f and the unit normal $\mathbf{N}_f$ by

$$A_f = \left|\mathbf{A}_f\right|, \qquad \mathbf{N}_f = \frac{\mathbf{A}_f}{A_f}. \quad (3)$$

Observing that the flux of a constant vector field $\mathbf{u}$ through the face f is expressed as $\mathbf{A}_f\cdot\mathbf{u}$, we can interpret these definitions geometrically: $\mathbf{N}_f = \mathbf{u}$ is the unit vector producing the maximum flux across the face, and A_f is the maximal value of the flux.

Once the area of a face is defined, the energy of a nonplanar configuration of vertices can be computed. The usual first three terms on the right-hand-side of Eq. 1 penalize bending deformations only weakly, see Results. They produce a bending modulus for the epithelial sheet that is entirely determined by the two-dimensional (2D) biophysical parameters $(A^0 = 1, G, H)$ and that moreover depends on the somewhat arbitrary definition of the discrete area $\mathbf{A}_f$. Therefore, to produce a better defined model, adaptable to diverse biological contexts, we have added the last term in the right-hand-side of Eq. 1. It is a discrete bending energy: the dot product is the cosine of the angle between the normals to adjacent cells and so, for small deflections, the parenthesis grows as one half of the square of this angle. This term tends to keep normals of adjacent cells aligned, much like spins in the classical Heisenberg model of ferromagnetism (20). This bending energy has been used in previous work to model elastic shells using triangulated surfaces (21,22), and it has been shown to be equivalent to the usual bending energy in the continuous limit (23). We will show in the following that a suitable choice of B allows one to adjust the vertex model rigidity to match that of the tissue under consideration.

Contractile contour

An additional contractile contour in the epithelium is implemented in the vertex model through the additional energy term,

$$\mathcal{E}_\Gamma = \Gamma\sum_{e\in C} L_e. \quad (4)$$

The geometry of the lattice is defined by two integers P_1 and P_2 with $0<P_1<P_2$, see Fig. 2 *A*: the diameter of the contour C is $(2P_1 + 1)$ cells, and the diameter of the entire lattice is $(2P_2 + 1)$ cells. The number of cells inside the contractile contour C is $n_1 = 1 + 3P_1(P_1 + 1)$, and the total number of cells is $n_2 = 1 + 3P_2(P_2 + 1)$.

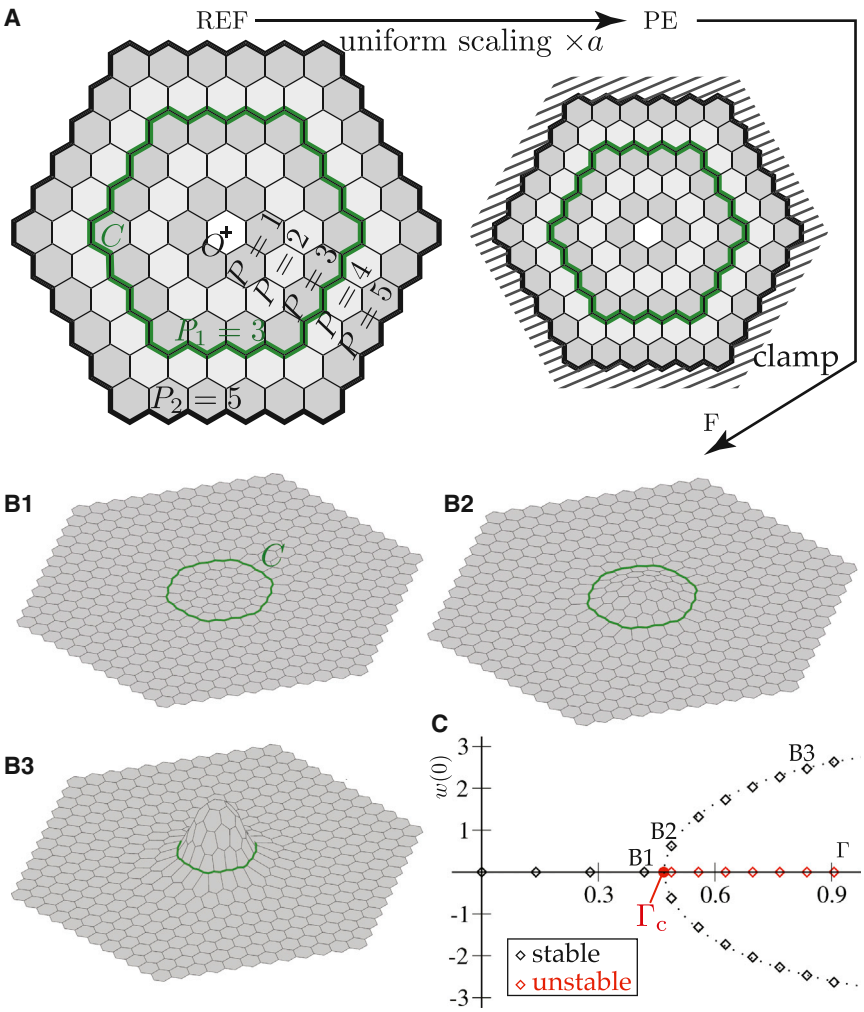

FIGURE 2 Buckling in the vertex model driven by a contractile contour C. (*A*) Starting from the reference configuration REF, here with geometrical parameters $(P_1, P_2) = (3, 5)$, a uniform scaling a is applied until a planar equilibrium PE is reached; then, the outer boundary is clamped, and we track 3D equilibrium solutions F. (*B1–B3*) Three equilibrium configurations with $(G, H, B) = (0.254, 0, 0.0534)$ and $(P_1, P_2) = (3, 11)$: (*B1*) below threshold, $\Gamma = 0.418$; (*B2*) just above the threshold, $\Gamma = 0.488$; and (*B3*) well above threshold, $\Gamma = 0.836$. (*C*) Bifurcation diagram displaying buckling threshold $\Gamma_c = 0.468$. Dotted curve is a guide to the eye. To see this figure in color, go online.

Numerical method

With the aim to investigate the effect of the contractile contour, we have implemented a C++ code to solve the vertex model numerically: the code solves the equilibrium using Newton-Raphson iterations, by cancelling the residual force vector on all vertices. This employs the Armijo line search (24) featuring quadratic convergence. The code relies on the armadillo C++ linear algebra library (25). It is initialized with the reference configuration REF, such that cells have unit area, $A^0 = 1$. For $\Gamma = 0$ and with a free outer boundary, the sheet shrinks to a planar flat equilibrium configuration with uniform cell size (configuration PE). Next, the inhomogeneous contractile force Γ is increased in small steps, with vertices lying along the tissue boundary immobilized at the position found in configuration PE: this yields configurations F indexed by the value of Γ, which can be planar or nonplanar.

Linear stability

In addition, we investigated the stability of equilibria by computing their tangent stiffness matrix, which is the Hessian matrix of the energy with respect to vertex position or, equivalently, minus the jacobian matrix of the residual force. If the sign of the smallest (real) eigenvalue of this matrix is positive, the equilibrium is stable under energy-minimizing dynamics. If it is negative, the equilibrium is unstable. The jacobian is calculated using finite differences, and its smallest eigenvalue and the corresponding eigenvector are obtained via inverse power iterations (24). When Γ passes Γ_c, the planar equilibria become unstable: we compute buckled solutions by perturbing the planar solution along the leading eigenvector of the stability analysis.

Homogenization of a hexagonal lattice

We propose a derivation of a continuous plate model from the vertex model. It is based on a variant of the Cauchy-Born rule for hexagonal lattices, which we briefly review next.

The Cauchy-Born rule (26,27) is applicable to the analysis of simple Bravais lattice. It considers homogeneous deformations $\mathbf{x}_v = \mathbf{F}\cdot\mathbf{X}_v$, where $\mathbf{X}_v$ is the reference position of the vertex v (or the atom v in a crystal), $\mathbf{x}_v$ is actual position, and $\mathbf{F}$ is an arbitrary deformation gradient. For a sheet embedded in the Cartesian 3D space, $\mathbf{F}$ is a 3×2 matrix. The homogenization is carried out by calculating the energy of the lattice in terms of the invariants of $\mathbf{F}$, and by identifying the result with an elastic energy. This captures the energy of configurations such that the deformation gradient varies on a length-scale much larger than the lattice parameter L^0.

We consider a hexagonal lattice, which is made up of two sublattices. For complex lattices such as this one, the Cauchy-Born rule must be extended to allow for an independent translation of its sublattices, see for instance (26). For the hexagonal lattice, this reads $\mathbf{x}_v = \mathbf{F}\cdot\mathbf{X}_v \pm (\mathbf{p}/2)$, where $\mathbf{p}$ is a vector

called the microscopic shift and the sign $\pm$ is alternating depending on which one of the two sublattices of the vertex v belongs to, see Fig. S1 in the Supporting Material. Note that the vertices are not in equilibrium except for a special value of $\mathbf{p}$, usually nonzero, depending on the macroscopic deformation gradient. The first and second gradients of the energy with respect to $\mathbf{p}$ define a stress and moduli, respectively, and this is known as inner elasticity (26). In this context, $\mathbf{F}$ is a macroscopic deformation gradient and we call $\pm(\mathbf{p}/2)$ the microscopic displacement. The homogenization is then carried out by expressing the energy in terms of $\mathbf{F}$ and $\mathbf{p}$, minimizing it with respect to $\mathbf{p}$ (relaxation step), and identifying the relaxed energy, now a function of $\mathbf{F}$, with that of an equivalent elastic continuum.

This procedure captures the dependence of the energy on the first gradient $\mathbf{F}$, but is unable to account for bending of the sheets that depend on curvature, i.e., on the second gradient of displacement. The Cauchy-Born rule must be extended one more time to capture the bending energy of a 2D lattice—this question has received considerable interest recently for the analysis of single-walled carbon nanotubes, see for instance (28–30). The two-sublattice structure of the hexagonal lattice is also well-known to lie at the root of the peculiar band structure of graphene (31). Extensions of the Cauchy-Born rule have been proposed to deal with curvature, by means of the exponential map (32) or by pushing the expansion of the displacement to second order (29,30).

We propose a simpler method, which is particularly suited to the analysis of small perturbations near a planar configuration (in what follows, we indeed relax the residual stress in the lattice by means of a uniform stretching $a\,\mathbf{X}$, and analyze small perturbations near this configuration). All equations are systematically linearized with respect to the amplitude of the perturbation. In this linear context, one can treat the various Fourier modes separately. Therefore, we assume that the macroscopic position is $\mathbf{x}_v^{\text{macro}} = a\,\mathbf{X}_v + \Re(\widehat{\mathbf{u}}\,e^{i\,\mathbf{k}\cdot\mathbf{X}_v})$, and that the microscopic displacement reads $\mathbf{u}_{\text{micro}} = \pm\Re((\widehat{\mathbf{p}}/2)\,e^{i\,\mathbf{k}\cdot\mathbf{X}_v})$. Here, $\Re$ denotes the real part, $\widehat{\mathbf{u}}$ and $\widehat{\mathbf{p}}$ are complex vectors capturing the macroscopic and microscopic perturbations, respectively, and $\mathbf{k}$ is the wavevector. Note that in the linear setting, only microscopic and macroscopic displacements corresponding to the same wavenumber $\mathbf{k}$ can be coupled. Summing the two contributions, we consider deformed configurations of the form

$$\mathbf{x}_v \;=\; a\,\mathbf{X}_v + \Re\left(\left(\widehat{\mathbf{u}} \pm \frac{\widehat{\mathbf{p}}}{2}\right) e^{i\,\mathbf{k}\,\cdot\,\mathbf{X}_v}\right). \qquad (5)$$

Our homogenization method is carried out by considering the limit $|\mathbf{k}|\to 0$, combining with appropriate scaling assumptions on $\widehat{\mathbf{u}}$ and $\widehat{\mathbf{p}}$, and calculating an expansion of the energy in terms of $\widehat{\mathbf{u}}$ and $\widehat{\mathbf{p}}$. This is done in the Supporting Material and summarized in the next section.

RESULTS

Continuous elastic plate approximation

The vertex model provides a quantitative description of the forces produced at the cell level in response to deformation. For weakly deformed cells, these forces increase linearly with the deformation. Thus, at the tissue level, one expects the epithelium to behave like an elastic sheet when the cells are weakly deformed (but the global deformation of the tissue can nonetheless be important). Our aim is to support this intuition by an explicit calculation and, importantly, to quantitatively relate the sheet elastic moduli to the cell level parameters G, H, and B. We thus analyze below the energy changes associated with macroscopic deformations that vary on scales large compared with the cell size, such that the cells are weakly deformed. We proceed in two steps. We first determine the equilibrium planar configuration for the regular epithelium that we consider, building up on previous studies (3,13) that investigated this question. We then examine the energy costs associated with nonplanar deformations of this equilibrium configuration. A simple example of the long-wavelength approximation in a cell-modeling context is provided by (33), where the approximation is used in one dimension.

We restrict ourselves to an epithelium consisting of identical, hexagonal cells ($n = 6$). Thus, the reference vertex configuration is a regular hexagonal lattice with faces having unit area $A^0 = 1$. From planar geometry, the edge length of this reference lattice is $L^0 = \sqrt[4]{4/27}$. The line tension (term proportional to G in the energy) and the perimeter elasticity (proportional to H) both induce in-plane stress in the lattice. If the lattice is not held by boundary conditions, it relaxes this stress and assumes an equilibrium configuration of minimal energy. We seek this minimal energy configuration as a uniformly scaled hexagonal lattice, with cells of area a^2 and edges of length $(a\,L^0)$. In this planar equilibrium configuration, the energy per cell reads as follows:

$$\epsilon_{\text{PE}}(a) \;=\; \frac{1}{2}\left(1-a^2\right)^2 + \sqrt{2}\sqrt[4]{3}\,a\,G + 4\sqrt{3}\,a^2\,H. \qquad (6)$$

When the energy $\epsilon_{\text{PE}}(a)$ is at its minimum, a is a root of $\epsilon'_{\text{PE}}(a) = 0$. Depending on the values of the parameters G and H, this equation may have zero, one, or several positive roots a. The absence of a positive root signals the absence of an equilibrium configuration: the area elasticity term is too weak to counterbalance the line tension and the perimeter elasticity, and the lattice collapses (see (13) for details). When multiple roots exist, we consider the only one that corresponds to a minimum of $\mathcal{E}_{\text{vm}}$. To avoid solving the cubic equation $\epsilon'_{\text{PE}}(a) = 0$ for a, we view a as a free parameter and G as a dependent variable, and solve the equation for G instead in the following:

$$G(a) \;=\; a\frac{\sqrt{2}}{\sqrt[4]{3}}\left(1-a^2-4\sqrt{3}H\right). \qquad (7)$$

Consider now a small perturbation from this planar equilibrium configuration PE, resulting in a *final* configuration F. Because the hexagonal lattice is not a simple Bravais lattice, this perturbation is the sum of a smooth macroscopic displacement, and a rapidly oscillating microscopic displacement, see Materials and Methods. We denote by $\mathbf{x}_v = a\,\mathbf{X}_v + v_X(\mathbf{X}_v)\,\mathbf{e}_X + v_Y(\mathbf{X}_v)\,\mathbf{e}_Y + w(\mathbf{X}_v)\,\mathbf{e}_Z$ the macroscopic deformed position of a vertex, as obtained by averaging out the oscillatory microscopic displacement. The microscopic displacement is not included in tihs particular equation (see the microscopic analysis below and in the Supporting Material), but is correctly accounted for by our effective elastic moduli. Note that the displacement (v_X, v_Y, w) is sought as a function of the Lagrangian variable $\mathbf{X}_v$, the vertex position in reference configuration. As

summarized below and detailed in the Supporting Material, we find that the energy of the lattice in the final configuration F is described by an elastic plate model in the continuous limit, $\mathcal{E}_{\rm vm} \approx \mathcal{E}_{\rm plate}$ where

$$\mathcal{E}_{\rm plate} = \frac{1}{2}\iint \left(\lambda\, {\rm tr}^2\mathbf{E} + 2\mu\left|\mathbf{E}^2\right| + \beta(\Delta w)^2\right) {\rm d}X\, {\rm d}Y, \quad (8)$$

where $\mathbf{E}$ denotes the macroscopic Cauchy-Green tensor measuring stretching (34,35), $\left|\mathbf{E}^2\right| = {\rm tr}(\mathbf{E}\cdot\mathbf{E})$ its invariant, and $w(X,Y) = \mathbf{x}\cdot\mathbf{e}_Z$ the lattice deflection along the Z-direction, i.e., away from the reference configuration lying in the (X,Y)-plane. The Laplacian operator in the bending term makes use of the reference coordinates, $\Delta = \partial^2/\partial X^2 + \partial^2/\partial Y^2$. The components of $\mathbf{E}$ read, for small deformations (the so-called Föppl-von Kármán approximation) (34,35), $E_{ij} = 1/2(\partial_i v_j + \partial_j v_j) + (1/2\, a)\partial_i w \partial_j w$, where the last term couples planar and nonplanar displacements and plays a crucial role in the analysis of buckling. Note that the simple form of Eq. 8 reflects our assumption of a small strain in the lattice plane.

To prove the equivalence $\mathcal{E}_{\rm vm} \approx \mathcal{E}_{\rm plate}$, we need only consider a single, representative cell (in the Supporting Material, this is the central cell). We consider a trial displacement of the form given in Eq. 5, obtained by the superposition of a uniform stretch with ratio a bringing the lattice to a stressfree configuration PE, a smooth (macrosopic) displacement captured by the complex amplitude vector $\widehat{\mathbf{u}}$, and an oscillatory (microscopic) displacement captured by the complex shift vector $\widehat{\mathbf{p}}$. Both the macroscopic and microscopic displacement are modulated harmonically with a 2D wavevector $\mathbf{k} = \eta\,\mathbf{K}$, where $\eta \to 0$ is an expansion parameter. We show in the Supporting Material that the energy of the vertex model is asymptotically equivalent to that of the plate model in the long wavelength limit, $\eta \to 0$. To do so, we find the optimum microscopic displacement $\widehat{\mathbf{p}}$ corresponding to a prescribed macroscopic displacement $\widehat{\mathbf{u}}$, insert the result into the energy of the vertex model, and we identify the relaxed energy with the continuous plate energy in Eq. 8.

The identification yields the following expressions for the stretching moduli λ and μ and for the bending modulus β (see the Supporting Material):

$$\lambda = -1 + 2\,a^2 + 2\sqrt{3}\,H \quad (9a)$$

$$\mu = \frac{1}{2}\left(1 - a^2\right) \quad (9b)$$

$$\beta = \frac{\sqrt{3}}{a^2}B + \frac{1 - a^2}{8\sqrt{3}}. \quad (9c)$$

These expressions for the Lamé coefficients λ and μ correct those derived by Staple (13) in the planar case (see the Supporting Material for details). With Eqs. 9a–9c, we have completely specified the plate model toward which the vertex model converges in 3D. The conditions warranting that the plate energy is positive definite (material stability) are discussed in the Supporting Material: for instance, when $H = 0$, stability requires $0 < G < 0.4136$.

The limit where both G and H are small is worthy of attention, as a is then close to 1 by Eq. 7. This brings in two simplifications: 1) the mapping from the reference to the equilibrium configuration is infinitesimal and so there is no need to distinguish between these configurations; and 2) the expressions of the moduli can be linearized with respect to the small quantities G, H, and $(1 - a)$. This yields the following:

$$G_{\rm lin} = \frac{2\sqrt{2}}{\sqrt[4]{3}}\left((1 - a) - 2\sqrt{3}H\right) \quad (10a)$$

$$\lambda_{\rm lin} = 1 + \left(2\sqrt{3}H - 4(1 - a)\right) \quad (10b)$$

$$\mu_{\rm lin} = 1 - a \quad (10c)$$

$$\beta_{\rm lin} = \sqrt{3}B + \frac{1 - a}{4\sqrt{3}}. \quad (10d)$$

In this limit, $\lambda_{\rm lin}$ converges to 1 but $\mu_{\rm lin}$ goes to zero: as a result, the plate model tends to preserve area (this is obvious from the discrete Eq. 1 because the area term becomes formally dominant over the other terms that provide shear and bending resistance). For 2D deformable bodies, Poisson's ratio reads $\nu = \lambda/(2\mu + \lambda) \approx 1 - 2(1 - a)$ and is indeed close to the area-preserving limit $\nu = 1$ (2D incompressibility). Another interesting fact is that the homogenized bending modulus $\beta_{\rm lin}$ has two contributions, see Eq. 10d: the first one, $\sqrt{3}\,B$, is independent of a but disappears if the discrete bending term is omitted in the model ($B = 0$); the second term, $(1 - a)/(4\sqrt{3})$, which we call a residual bending modulus, is present even if $B = 0$. It is impossible to bend a hexagonal mesh while preserving all edge lengths and face areas: it is said to be geometrically rigid. The energy of the vertex model must therefore increase when the configuration goes from planar to nonplanar, even when no explicit bending energy is considered (i.e., even for $B = 0$): this gives rise to the residual bending modulus. In real epithelia, the geometric rigidity of the mesh is likely irrelevant and there are many other mechanisms that lead to an effective bending rigidity, including 3D deformations of the cells, and the stiffness of the surrounding tissues. The role of the explicit coefficient B included in the extended vertex model is to effectively capture all these mechanisms.

To summarize, we have shown that the extended vertex model is equivalent to a thin plate in the long-wavelength limit, and have identified the elastic moduli of the equivalent plate. The case where the parameter a is close to 1 is

particularly simple: then, the mesh almost preserves area and simpler expressions for the moduli have been derived. We have identified a small residual bending rigidity having a geometrical origin when $B = 0$, and we have argued that the explicit bending term that we introduced in Eq. 1 allows for a more realistic and better controlled description of bending in real epithelia.

A test case: buckling driven by tissue inhomogeneity

Planar vertex models have successfully been used to capture experimental phenomenology, such as the influence of mechanically driven cell rearrangements on epithelial cell patterns and morphogenesis (3,4) as well as to infer epithelial tissue internal stresses (6,36) and to examine their influence on cell proliferation (12). A recent study (17), which motivated our work, has initiated the use of vertex models for the study of nonplanar epithelium deformations. Specifically, appendage formation in *D. melanogaster* has been attributed to the 3D deformations of the fly egg follicle epithelium caused by in-plane forces; simulations of a vertex model featuring an inhomogeneous distribution of line tension produced buckled shapes that compared well with real epithelia.

In this section, we use a variant of the geometry from (17) to test both our vertex model and our continuous plate model. We show that the simulation results are very sensitive to the value of the bending modulus B, although this modulus has been ignored in previous work. We also show that the continuous plate model can be used to rationalize the behavior of the vertex model: the continuous model features buckled solutions similar to those of the discrete model in the presence of an inhomogeneous line tension, and yields an accurate prediction for the buckling threshold as a function of all the parameters of the problem.

Numerical investigation

A simplified version of the geometry considered in (17) is sketched in Fig. 2 *A*. A contractile contour C is embedded inside a lattice. It represents the actin cable observed in the experiments, which displays a high concentration of the motor protein myosin (17). In our model, the edges belonging to the contour are assigned a line tension $(G + \Gamma)$ that is larger than the line tension G of the other edges, see Materials and Methods for details.

We carry out a numerical and analytical buckling study based on the total energy $\mathcal{E}_{\rm vm} + \mathcal{E}_{\Gamma}$, when the inhomogeneity of the line tension Γ is progressively (and uniformly) increased.

Given the values of the parameters (G, H, B) of the extended vertex model, we first let the lattice relax to its planar equilibrium configuration PE, by applying a uniform scaling a such that $\epsilon'_{\rm PE}(a) = 0$. Next, we clamp the outer boundaries by restraining the motion of the outer vertices in all directions. Finally, we increase Γ progressively and track the equilibrium shapes of the inhomogeneous lattice numerically using Newton–Raphson iterations. Their stability is examined using standard eigenvalue analysis (see Materials and Methods for details). When the inhomogeneity Γ is smaller than some threshold Γ_c, the equilibrium solution remains planar, albeit nonhomogeneous: the contractile contour tends to become circular, and the region inside the contour is compressed, see Fig. 2 *B1*. Beyond the threshold value Γ_c, this planar solution becomes unstable, and a pair of stable nonplanar solutions appears (Fig. 2, *B2* and *C*). These buckled solutions are mirror-symmetric to each other, with respect to the clamping plane $z = 0$. When plotted as a function of the control parameter Γ, the maximum deflection $w(0)$ traces out a bifurcation diagram that is typical of a supercritical pitchfork bifurcation, see Fig. 2 *C*, and is similar to that of the well-studied Elastica, see, e.g., (34,35). In particular, the maximum tissue deflection grows like $\sqrt{\Gamma - \Gamma_c}$ close to threshold.

Buckling in the plate model

The reported simulations show that inhomogeneous tissue properties can lead to buckling, and that the extended vertex model captures this phenomenon. We now show that a detailed account of this buckling phenomenon is possible based on the continuous plate model obtained earlier via homogenization. To this end, we introduce a variant of the buckling problem in a continuous, axisymmetric geometry, see Fig. 3 *A*.

We consider the limit $G, H, \Gamma \ll 1$ and $a \approx 1$ where the homogenized plate model almost preserves areas, and strains remain small. Using these assumptions, the buckling analysis can be carried out analytically using the Föppl-von Kármán equations for plates. The extension of the buckling analysis to finite values of G, H, Γ is straightforward but requires numerical integration. The problem is similar to the budding of a domain in a membrane driven by line tension at the domain edge that was treated using approximate energy considerations in (37,38). The highly strained limit where sharp localized folds appear would also be interesting to study. However, this would require entirely different techniques and it lies beyond the scope of this study.

We define the inner and outer radii R_1 and R_2 for our continuous problem by matching the areas in the reference configurations: πR_1^2 is matched with the number of cells inside the contour, n_1, and πR_2^2 with the total number of cells, n_2: $R_1 = f(P_1)$ and $R_2 = f(P_2)$ where $f(P) = \sqrt{(1 + 3P(P+1))/\pi}$ and P_1 and P_2 are integers measuring the radius of the contractile contour and of the outer tissue boundary, see Fig. 2 *A* and Materials and Methods. Note that $f(P) \approx P + 1/2$ to within 3% for any value of P. As a result, R_1 and R_2 are close to the average radii of the contour C and of the external boundary, respectively.

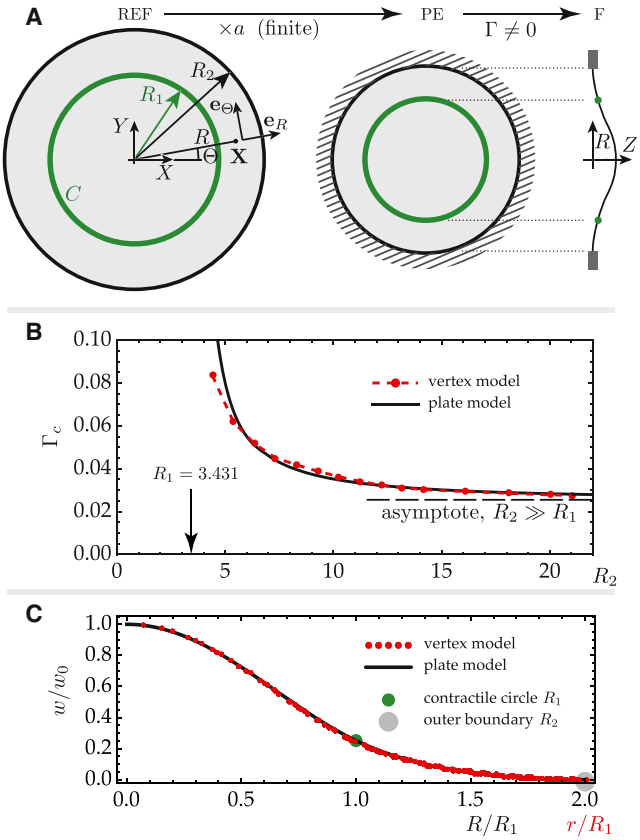

FIGURE 3 Buckling in the continuous setting, and comparison with results of the vertex model for $(G,H,B) = (0.0351, 0, 0.00738)$. (*A*) Equivalent continuous, axisymmetric geometry; buckling of a circular plate having a clamped outer edge, subjected to contraction along an embedded circle (*green*). The buckled configuration F is represented after cutting through the plane (ORZ) containing the axis of symmetry. (*B*) Buckling threshold as a function of the outer radius R_2 with fixed inner radius $R_1 = 3.431$. (*C*) Comparison of the shapes $w(R)$ of the buckling modes rescaled by the deflection w_0 at the center, with $(P_1, P_2) = (8, 16)$ in the vertex model and $\alpha = R_2/R_1 = 2$ in the plate model, immediately above the buckling threshold $\Gamma = 0.0217 > \Gamma_c = 0.0194$. For the vertex model, each data point corresponds to a simulation vertex, with r being its distance to axis (Oz) and w its deflection, both measured in buckled configuration. Because G is small and $H = 0$, we use the linearized moduli in the plate model for (*B*) and (*C*). To see this figure in color, go online.

In axisymmetric geometry, the displacement and strain are functions of the radial coordinate $R = \sqrt{X^2 + Y^2}$, and independent of the polar angle Θ. We denote by $(\mathbf{e}_R(\Theta), \mathbf{e}_\Theta(\Theta))$ the local polar basis, and we seek the displacement in the axisymmetric form $\mathbf{u}(R,\Theta) = v(R)\,\mathbf{e}_R(\Theta) + w(R)\,\mathbf{e}_Z$ for $0<R<R_2$. By symmetry, the Cauchy-Green strain writes $\mathbf{E} = E_R\,\mathbf{e}_R \otimes \mathbf{e}_R + E_\Theta\,\mathbf{e}_\Theta \otimes \mathbf{e}_\Theta$, where the Föppl-von Kármán expression of the principal strain is used, $E_R = v'(R) + w'^2(R)/2$ and $E_\Theta = v(R)/R$.

We introduce a continuous approximation of the discrete energy of the contractile circle,

$$\mathcal{E}_\Gamma \;=\; 2\,\pi\,\Gamma\,R_1(1 + E_\Theta(R_1)). \tag{11}$$

As in the discrete setting, see Eq. 4, the perimeter of the deformed contractile circle, $2\pi\,R_1(1 + E_\Theta)$, is multiplied by the line tension Γ. We solve the circular plate buckling problem by minimizing the total energy $\mathcal{E}_{\text{plate}} + \mathcal{E}_\Gamma$, using the linearized expressions of the moduli in Eq. 10.

We start by considering a planar solution, $w(R) = 0$, which we use as the base solution for our buckling analysis. The complete solution of this planar, axisymmetric problem of linear elasticity is worked out in the Supporting Material. The stress obtained in this way is called the prestress. Its principal values are denoted by $S_R(R)$ and $S_\Theta(R)$. In the limit of 2D incompressibility that we consider here $(a \approx 1)$, the solution is particularly simple:

$$S_R(R) \;=\; S_\Theta(R) \;=\; -S^*\,t(R)$$
$$\text{where } t(R) \;=\; \begin{cases} 1 & \text{if } R<R_1 \\ -\dfrac{1}{\alpha^2 - 1} & \text{if } R_1<R \end{cases}, \tag{12}$$

where $\alpha = R_2/R_1$ is a geometrical parameter, and $S^* = ((\alpha^2 - 1)/\alpha^2)(\Gamma/R_1)$ is a typical membrane stress. In the limit considered, the prestress is locally isotropic, piecewise constant, and independent of the elastic moduli. It is compressive in the interior region $R<R_1$ (where $S_R = S_\Theta < 0$), which drives the buckling instability, and tensile in the outer region $(S_R = S_\Theta > 0)$.

We can now proceed to investigate the axisymmetric buckling of the plate using linear stability analysis. In axisymmetric geometry, the equation for the transverse equilibrium of the plate obtained by variation of the energy in Eq. 8 reads, when linearized near the prestressed configuration, see for instance (39,40):

$$\beta_{\text{lin}}\left(-\frac{1}{R}\frac{\mathrm{d}(R\,q')}{\mathrm{d}R} + \frac{q}{R^2}\right) - S^*\,t(R)\,q(R) \;=\; 0, \tag{13}$$

where $q(R) = w'(R)$ is the radial slope. The boundary conditions are the continuity condition $q(0) = 0$, and the clamping condition $q(R_2) = 0$ (the clamping condition on the outer edge arises when going from the hexagonal to the perfectly axisymmetric geometry, see the Supporting Material). When solutions $q(R)$ exist, this indicates that the buckling load has been reached. This stability problem depends solely on the dimensionless geometric parameter $\alpha = R_2/R_1$ and on the dimensionless tension $\gamma = S^*\,R_1^2/\beta = (\Gamma\,R_1/\beta)((\alpha^2 - 1)/\alpha^2)$.

We conclude that buckling occurs when γ reaches a critical value that is a function of the aspect-ratio α only, $\gamma = \gamma_c(\alpha)$. The function $\gamma_c(\alpha)$ can be found by solving Eq. 13 in terms of Bessel functions in the inner $(R<R_1)$ and outer $(R>R_1)$ regions, and matching them across the contractile circle $R = R_1$, see the Supporting Material. The dimensionless buckling threshold varies in the range

$\gamma_c(\alpha = \infty) = 5.78$ when clamping is applied at infinity ($R_2 \gg R_1$), to $\gamma_c(\alpha = 1) = 14.68$ when clamping is applied immediately outside the contracting circle ($R_2 = R_1$) as in the analysis of circular delamination blisters (40). Our analysis also provides the exact solution for the budding of a membrane domain driven by line tension considered in (38) (the approximate analysis of (38) considered a spherical cap budding from a plane and ignored the bending energy in the circular ridge; it predicted a dimensionless buckling threshold equal to 8 and a subcritical transition, in contrast to what we find here).

Finally, we compare the results of our buckling analysis for the plate model with the numerical results obtained with the extended vertex model, limiting ourselves to the case $H = 0$ for simplicity. Expressing β_{lin} in terms of the parameters of the vertex model by Eqs. 10d and 10a, we predict a buckling threshold $\Gamma = \Gamma_c$, for $H = 0$ in the following:

$$\Gamma_c = \gamma_c(\alpha)\frac{\alpha^2}{\alpha^2 - 1}\frac{1}{R_1}\left(\frac{G}{8\sqrt{2}\sqrt[4]{3}} + \sqrt{3}\,B\right). \qquad (14)$$

Fig. 3 *B* displays the buckling threshold versus tissue size $R_2 = \alpha R_1$ as predicted by this equation, together with our numerical results for the vertex model. Despite the simplification of a radially symmetric, continuous geometry, the plate model closely agrees with the discrete simulation results. The buckling threshold decreases with the tissue size R_2 and quickly reaches an asymptote $\Gamma_c = \Gamma_c^{\infty}$. This decrease is because the clamp on the outer boundary hinders the buckling, but this finite size effect quickly fades out as $\alpha = R_2/R_1$ becomes larger than ≈ 2. We observed similar agreement between the analytical results and the vertex model simulations when other geometric or material parameters were varied. In particular, Fig. S3 demonstrates the existence of a residual modulus in the vertex model for $B = 0$ (thus a nonzero buckling threshold Γ_c) and shows that the dependence of the buckling threshold Γ_c on the bending modulus B predicted by Eq. 14 is accurate. The mode shape is predicted with excellent accuracy by the continuous plate model as well (see Fig. 3 *C*). Note that we have compared the buckling threshold and the rescaled mode shapes, but not the buckling amplitudes: to predict the buckling amplitude based on the plate model (for comparison with the data shown in Fig. 2 *C*), a weakly nonlinear analysis or a nonlinear simulation of the plate model are required. This goes beyond the linear analysis presented in this study. Observe that the solution shown in Fig. 2 *B3* displays large strain and large curvature; the assumptions of our linearly elastic plate model are not justified in this deeply postbuckled regime.

Finally, we note that an experimental test of relation (Eq. 14) would require measuring the cable tension and bending rigidity. Inhomogeneities in line tension can be assessed by recoil after laser-cutting experiments (1). Line tension can also be quantitatively measured by dynamic tissue perturbations with optical tweezer, a recently developed technique (41). This technique also appears very appropriate for direct measurement of the bending rigidity.

DISCUSSION

In this work, we have proposed an extended vertex model for studying nonplanar epithelial deformations, including explicitly a discrete bending energy. We have shown that this model reduces to the usual elastic plate description in the limit of a long wavelength compared with the scale of a single cell. We used a systematic method for deriving the plate model, which can be extended to other types of mesh and energy function.

For simple lattices, the traditional Cauchy-Born approximation assumes that the vertex displacements are given by a linear mapping. The hexagonal network being a complex lattice in the sense of Bravais, the Cauchy-Born approximation has been extended by introducing a shift $\mathbf{p}$ capturing the relative translation of the two sublattices: the associated microscopic displacement has alternating signs from one vertex to its neighbors. In the context of Fourier analysis, we have calculated the complex shift $\hat{\mathbf{p}}$ in terms of the complex amplitude $\hat{\mathbf{u}}$ of the macroscopic (averaged) displacement: as a result, our homogenized plate moduli correctly take into account the microscopic oscillatory displacement, even though there is no need to account for it in the continuous plate model. A clear—although unintentional—demonstration of the existence of this microscopic displacement is given in (42), where the authors impose an affine displacement to all vertices lying on the boundary of a 2D rectangular patch. These conditions are incompatible with the existence of an oscillatory microscopic displacement; effectively, they impose $\mathbf{p} = 0$ along the boundary. As a result, they obtain a nonaffine solution, which we can describe as follows in light of our analysis: the solution described by the generalized Cauchy-Born rule (homogeneous solution plus oscillatory displacement, $\mathbf{p} \neq 0$) is reached deep in the interior of the domain and a boundary layer builds up to connect the interior with the domain boundary, where $\mathbf{p} = 0$. This boundary layer is a few cells thick and could be described quantitatively by accounting for the strain energy associated with the gradient of $\mathbf{p}$, see for instance (29).

We have also applied the discrete vertex model and the continuum plate model to 3D epithelial deformations by investigating the buckling of an epithelial sheet induced by a contracting circle. In both descriptions, we have found a supercritical bifurcation at a well-defined threshold, and the plate model enabled us to capture the dependence of the buckling threshold on the model parameters. Our analysis of buckling made use of several approximations, like that of an axisymmetric geometry and of small deformations, whereas the numerics were performed in a hexagonal

geometry that produced some regions of high strain. Moreover, we ignored the fact that the clamp on the outer boundary and the contractile circle both tend to force the microscopic displacement $\hat{\mathbf{p}}$ toward a non-equilibrium b value. Despite these simplifying assumptions, the plate model was found to account quite accurately for the numerical results of the vertex model. Therefore, we expect that our work will prove useful for the analysis of buckling in different contexts, as in the case of budding membrane domains (38). Our results for a contractile circle show that the buckling threshold quickly asymptotes to a limiting value as the size of the outer ring is increased. Buckling in a given region is thus localized and independent of morphogenetic events taking place elsewhere in the tissue. As a result, a large tissue could be morphed into a complex shape by the superposition of multiple buckling events in different regions. The simplest instance of this mechanism was previously found in (17) for the formation of dorsal appendage primordia in the Drosophila egg. We anticipate that other examples will be found, perhaps with the added complications of cell proliferation and deformation within the patch (43).

There are different interesting avenues for future development. One will consist in linking the phenomenological parameters of our cell model to those of more detailed, 3D cell-based descriptions, that, for instance, capture cell volume explicitly as in (44) or (45) (http://www.ncbi.nlm.nih.gov/pubmed/24367079). This would allow one to investigate how tissue rigidity arises and is regulated at the cell level. We also expect the proposed model and the demonstated link to continuum mechanics to be useful for the analysis of diverse biological problems where morphogenesis relies on cell mechanics (46). In this respect, it should be noted that the proposed vertex model can easily be modified to include spontaneous curvature (by introducing a nonzero rest angle between normals of neighboring cells). In this case, we expect buckling to appear via an imperfect pitchfork bifurcation. This is relevant for a whole family of biological problems where cells make use of differential apicobasal contractions, such as gastrulation (7). Finally, our results and methodology may prove interesting beyond biology in studying the folding and self-assembly of complex human-made elastic materials such as origami metamaterials (47,48).

SUPPORTING MATERIAL

Supporting Materials and Methods, five figures, Fourier analysis, and Mathematica source file are available at http://www.biophysj.org/biophysj/supplemental/S0006-3495(15)00504-4.

AUTHOR CONTRIBUTIONS

B.A., N.M., S.Y.S., and V.H. designed the research; B.A. and N.M. performed the research; B.A., I.G.K., and N.M. contributed analytic tools; B.A., N.M., S.Y.S., and V.H. wrote the article.

ACKNOWLEDGMENTS

N.M., S.Y.S., and B.A. acknowledge support from Grant RGP0052/2009 from the Human Frontiers Science Program. S.Y.S. also acknowledges support from the 1R01GM107103 grant from NIGMS. We are very grateful to the anonymous referee who pointed to us the need to account for the microscopic displacement in the derivation of the continuous model.

REFERENCES

1. Lecuit, T., P. F. Lenne, and E. Munro. 2011. Force generation, transmission, and integration during cell and tissue morphogenesis. *Annu. Rev. Cell Dev. Biol.* 27:157–184.
2. Martin, A. C., M. Gelbart, …, E. F. Wieschaus. 2010. Integration of contractile forces during tissue invagination. *J. Cell Biol.* 188:735–749.
3. Farhadifar, R., J.-C. Röper, …, F. Jülicher. 2007. The influence of cell mechanics, cell-cell interactions, and proliferation on epithelial packing. *Curr. Biol.* 17:2095–2104.
4. Rauzi, M., P. Verant, …, P. F. Lenne. 2008. Nature and anisotropy of cortical forces orienting Drosophila tissue morphogenesis. *Nat. Cell Biol.* 10:1401–1410.
5. Bosveld, F., I. Bonnet, …, Y. Bellaïche. 2012. Mechanical control of morphogenesis by Fat/Dachsous/Four-jointed planar cell polarity pathway. *Science.* 336:724–727.
6. Sugimura, K., and S. Ishihara. 2013. The mechanical anisotropy in a tissue promotes ordering in hexagonal cell packing. *Development.* 140:4091–4101.
7. Khan, Z., Y. C. Wang, …, M. Kaschube. 2014. Quantitative 4D analyses of epithelial folding during Drosophila gastrulation. *Development.* 141:2895–2900.
8. Honda, H. 1978. Description of cellular patterns by Dirichlet domains: the two-dimensional case. *J. Theor. Biol.* 72:523–543.
9. Honda, H. 1983. Geometrical models for cells in tissues. *Int. Rev. Cytol.* 81:191–248.
10. Sulsky, D., S. Childress, and J. K. Percus. 1984. A model of cell sorting. *J. Theor. Biol.* 106:275–301.
11. Graner, F., and Y. Sawada. 1993. Can surface adhesion drive cell rearrangement? Part II: a geometrical model. *J. Theor. Biol.* 164:477–506.
12. Hufnagel, L., A. A. Teleman, …, B. I. Shraiman. 2007. On the mechanism of wing size determination in fly development. *Proc. Natl. Acad. Sci. USA.* 104:3835–3840.
13. Staple, D. B., R. Farhadifar, …, F. Jülicher. 2010. Mechanics and remodelling of cell packings in epithelia. *Eur. Phys. J. E Soft Matter.* 33:117–127.
14. Fletcher, A. G., M. Osterfield, …, S. Y. Shvartsman. 2014. Vertex models of epithelial morphogenesis. *Biophys. J.* 106:2291–2304.
15. Méhes, E., and T. Vicsek. 2014. Collective motion of cells: from experiments to models. *Integr. Biol. (Camb).* 6:831–854.
16. Bardet, P. L., B. Guirao, …, Y. Bellaïche. 2013. PTEN controls junction lengthening and stability during cell rearrangement in epithelial tissue. *Dev. Cell.* 25:534–546.
17. Osterfield, M., X. Du, …, S. Y. Shvartsman. 2013. Three-dimensional epithelial morphogenesis in the developing *Drosophila* egg. *Dev. Cell.* 24:400–410.
18. Weaire, D., and N. Rivier. 1984. Soap, cells and statistics—random patterns in two dimensions. *Contemp. Phys.* 25:59–99.
19. Alexa, M., and M. Wardetzky. 2011. Discrete Laplacians on general polygonal meshes. *Trans. Graph. (SIGGRAPH 2011).* 30:102.
20. De Gennes, P., and C. Taupin. 1982. Microemulsions and the flexibility of oil/water interfaces. *J. Phys. Chem.* 86:2294–2304.
21. Kantor, Y., and D. R. Nelson. 1987. Crumpling transition in polymerized membranes. *Phys. Rev. Lett.* 58:2774–2777.
22. Kantor, Y., and D. R. Nelson. 1987. Phase transitions in flexible polymeric surfaces. *Phys. Rev. A.* 36:4020–4032.

23. Grinspun, E., Y. Gingold, …, D. Zorin. 2006. Computing discrete shape operators on general meshes. *Comput. Graphics Forum.* 25:547–556.
24. Burden, R., and J. Faires. 2011. Numerical Analysis, 9th ed. Cengage Learning, Boston, MA.
25. Sanderson, C. 2010. Armadillo: An Open Source C++ Linear Algebra Library for Fast Prototyping and Computationally Intensive Experiments. NICTA. *http://arma.sourceforge.net/armadillo_nicta_2010.pdf.*
26. Cousins, C. S. G. 1978. Inner elasticity. *J. Phys. C Solid State Phys.* 11:4867–4879.
27. Ericksen, J. L. 1984. The Cauchy and Born Hypotheses for crystals. *In* Phase Transformations and Material Instabilities in Solids. M. E. Gurtin, editor. Academic Press, New York, pp. 61–77.
28. Arroyo, M., and T. Belytschko. 2004. Finite crystal elasticity of carbon nanotubes based on the exponential Cauchy-Born rule. *Phys. Rev. B.* 69:115415.
29. Guo, X., J. B. Wang, and H. W. Zhang. 2006. Mechanical properties of single-walled carbon nanotubes based on higher order Cauchy-Born rule. *Int. J. Solids Struct.* 43:1276–1290.
30. Wu, J., K. C. Hwang, and Y. Huang. 2008. An atomistic-based finite-deformation shell theory for single-wall carbon nanotubes. *J. Mech. Phys. Solids.* 56:279–292.
31. Castro Neto, A. H., F. Guinea, …, A. K. Geim. 2009. The electronic properties of graphene. *Rev. Mod. Phys.* 81:109.
32. Arroyo, M., and T. Belytschko. 2002. An atomistic-based finite deformation membrane for single layer crystalline films. *J. Mech. Phys. Solids.* 50:1941–1977.
33. Fozard, J. A., H. M. Byrne, …, J. R. King. 2010. Continuum approximations of individual-based models for epithelial monolayers. *Math. Med. Biol.* 27:39–74.
34. Landau, L. D., and E. M. Lifshitz. 1981. Theory of Elasticity (Course of Theoretical Physics), 2nd ed. Pergamon Press, Oxford, UK.
35. Audoly, B., and Y. Pomeau. 2010. Elasticity and Geometry: From Hair Curls to the Non-linear Response of Shells. Oxford University Press, Oxford, UK.
36. Chiou, K. K., L. Hufnagel, and B. I. Shraiman. 2012. Mechanical stress inference for two dimensional cell arrays. *PLOS Comput. Biol.* 8:e1002512.
37. Helfrich, W. 1974. The size of bilayer vesicles generated by sonication. *Phys. Lett. A.* 50:115–116.
38. Lipowsky, R. 1992. Budding of membranes induced by intramembrane domains. *J. Phys. II.* 2:1825–1840.
39. Timoshenko, S., and J. Gere. 1961. Theory of Elastic Stability, 2nd ed. MacGraw Hill, New York.
40. Hutchinson, J., and Z. Suo. 1992. Mixed mode cracking in layered materials. *Adv. Appl. Mech.* 29:63–191.
41. Bambardekar, K., R. Clément, …, P.-F. Lenne. 2015. Direct laser manipulation reveals the mechanics of cell contacts in vivo. *Proc. Natl. Acad. Sci. USA.* 112:1416–1421.
42. Davit, Y., J. M. Osborne, …, J. Pitt-Francis. 2013. Validity of the Cauchy-Born rule applied to discrete cellular-scale models of biological tissues. *Phys. Rev. E Stat. Nonlin. Soft Matter Phys.* 87:042724.
43. Chauhan, B. K., M. Lou, …, R. A. Lang. 2011. Balanced Rac1 and RhoA activities regulate cell shape and drive invagination morphogenesis in epithelia. *Proc. Natl. Acad. Sci. USA.* 108:18289–18294.
44. Honda, H., M. Tanemura, and T. Nagai. 2004. A three-dimensional vertex dynamics cell model of space-filling polyhedra simulating cell behavior in a cell aggregate. *J. Theor. Biol.* 226:439–453.
45. Hannezo, E., J. Prost, and J.-F. Joanny. 2011. Instabilities of monolayered epithelia: shape and structure of villi and crypts. *Phys. Rev. Lett.* 107:078104.
46. Liang, H., and L. Mahadevan. 2011. Growth, geometry, and mechanics of a blooming lily. *Proc. Natl. Acad. Sci. USA.* 108:5516–5521.
47. Rammerstorfer, F., D. Pahr, …, W. Vonach. 2006. Buckling in thin walled micro and meso structures of lightweight materials and material compounds. *Comput. Mech.* 37:470–478.
48. Ryu, J., M. D'Amato, …, M. Dunn. 2012. Photo-origami—bending and folding polymers with light. *Appl. Phys. Lett.* 100:161908.

"From discrete to continuum models of three-dimensional deformations in epithelial sheets" Supporting Information

N. Murisic, et al.

May 15, 2015

S1 Detailed derivation of the homogenized plate model

We show that the energy of the vertex model introduced in the main text,

$$\mathcal{E}_{\rm vm} = \frac{1}{2}\sum_f (A_f - 1)^2 + G\sum_e L_e + \frac{H}{2}\sum_f {P_f}^2 + B\sum_{e'}(1 - \mathbf{N}_{f_1(e')}\cdot\mathbf{N}_{f_2(e')}), \tag{1}$$

is equivalent in the smooth limit to a plate energy, $\mathcal{E}_{\rm vm} \approx \mathcal{E}_{\rm plate}$, where

$$\mathcal{E}_{\rm plate} = \frac{1}{2}\iint \left(\lambda\ {\rm tr}^2\,\mathbf{E} + 2\,\mu\,|\mathbf{E}^2| + \beta\,(\Delta w)^2\right)\,{\rm d}X\,{\rm d}Y, \tag{2}$$

up to constant terms which we can ignore. We refer the reader to the main text for a definition of the various quantities entering in the vertex model. In the equivalent plate model, $\mathbf{E}$ is a macroscopic measure of stretching strain, see equation (14) below, w is the deflection and Δw is its Laplacian with respect to the Lagrangian coordinates (X, Y). The Lamé parameters λ and μ characterize the stretching behavior of the equivalent plate (μ being the shear modulus), and β is a bending modulus. These three parameters are expressed below in terms of the original parameters G, H and B, by identifying the two energies in the continuous limit.

In what follows, we omit the details of the calculations. They have been carried out using the symbolic calculation language Wolfram Mathematica [8]. The source code (notebook) is appended at the end of this document.

S1.1 Harmonic macroscopic and microscopic displacement (Cauchy-Born rule)

Let $\mathbf{X} = (X, Y)$ be the coordinates in reference configuration '0' of a vertex. Its position $\mathbf{x}$ in actual configuration is first scaled with ratio a, and then moved by a small macroscopic displacement plus a small microscopic displacement, see figure S1. The role of the uniform scaling is to relax the in-plane stress present in the configuration of reference, yielding the intermediate configuration 'PE' shown in the figure.

The Cauchy-Born rule provides a starting point for deriving a continuum description of lattices whose energy is the sum of interactions between neighbors. For simple Bravais lattices, the standard Cauchy-Born rule applies: a homogeneous deformation is applied onto the lattice. The hexagonal lattice, however, is a multi-lattice as it can be viewed as the union of *two* simple Bravais lattices. Therefore, the standard Cauchy-Born rule must be modified, see for instance [4]: a homogeneous deformation must be applied to each sub-lattice (with the same deformation gradient for all sub-lattices) and in addition, *a shift between them must be allowed*. This shift, called inner displacement, gives rise to an oscillatory displacement field which we refer to as the *microscopic displacement*. This shift is required for the equilibrium of all vertices to be satisfied. This approach based on homogeneous transformations works well when the energy of the

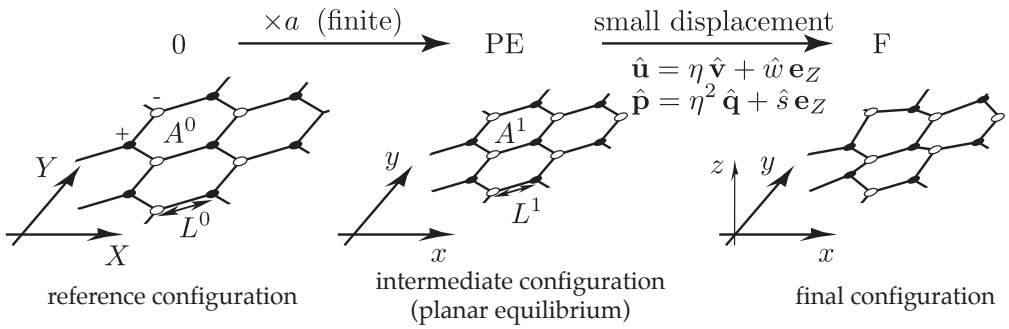

Figure S1: Analysis of the 3D vertex model combines a uniform scaling with ratio $a < 1$ from the reference configuration '0', and a small perturbation. The vertices are represented by filled and open disks depending on which Bravais sublattice they belong to. In the intermediate state 'PE', the edge length is $L^1 = a\,L^0$ and the face area is $A^1 = a^2\,A^0$. Using homogenization techniques, the energy of the final configuration 'F' given by the 3D vertex model (1) is identified to the energy of a thin elastic plate.

continuous model is a function of the deformation gradient only. To capture the higher-order derivatives associated with bending, extensions of the Cauchy-Born rule have been proposed [1, 2, 9]. Here, we propose a simpler approach, and assume that the displacement of the vertices belonging to each sub-lattice are harmonic functions of the position with a long wavelength. When combined with appropriate scaling assumptions on the large wavelength and on the small displacement, this makes the bending term appear naturally, as we show below. Another benefit of this approach is that it easily handles the dot product of unit normals in the bending term, even though this term cannot be easily written as a standard interaction term depending on the distances between neighboring vertices.

We assume that both the macroscopic and microscopic displacements are harmonic functions of the coordinates, see equation (5) in the main text:

$$\mathbf{x} = a\,\mathbf{X} + \Re\left(\left(\hat{\mathbf{u}} \pm \frac{\hat{\mathbf{p}}}{2}\right) e^{i\,\eta\,\mathbf{K}\cdot\mathbf{X}}\right). \tag{3}$$

Here, $\Re$ denotes the real part, $\mathbf{K} = (K_x, K_y)$ is a planar vector, η is a small real expansion parameter, $\mathbf{k} = \eta\,\mathbf{K}$ is the wavevector of the perturbation, and hats denote complex quantities: $\hat{\mathbf{u}}$ is a complex vector of dimension 3 representing the (smooth) macroscopic displacement, $\hat{\mathbf{p}}$ is a complex vector of dimension 3 representing the (oscillatory) microscopic displacement. The sign '$\pm$' is different for each sub-lattice: it is '$+$' for vertices marked with filled disks in figure S1, and '$-$' for vertices marked with open disks. As a result, the two sublattices are shifted with respect to one another by a microscopic shift vector $\Re\left(\hat{\mathbf{p}}\,e^{i\,\eta\,\mathbf{K}\cdot\mathbf{X}}\right)$.

In what follows, we consider the continuous limit $\eta \to 0$, where both the macroscopic displacement $\hat{\mathbf{u}}$ and the shift $\hat{\mathbf{p}}$ vary on a length-scale that is large compared to the mesh size. This is the asymptotic regime where the vertex model converges to a plate model.

The X and Y components of the complex amplitude vectors $\hat{\mathbf{u}}$ and $\hat{\mathbf{p}}$ correspond to in-plane perturbations, and their Z component to out-of-plane perturbations. For the energy to converge in the limit $\eta \to 0$, we need to make some scaling assumptions on these complex amplitudes. These read

$$\hat{\mathbf{u}} = \eta\,\hat{\mathbf{v}} + \hat{w}\,\mathbf{e}_Z \quad \text{and} \quad \hat{\mathbf{p}} = \eta^2\,\hat{\mathbf{q}} + \eta^2\,\hat{s}\,\mathbf{e}_Z \tag{4a}$$

where

$$\hat{\mathbf{v}} = \hat{v}_X\,\mathbf{e}_X + \hat{v}_Y\,\mathbf{e}_Y \quad \text{and} \quad \hat{\mathbf{q}} = \hat{q}_X\,\mathbf{e}_X + \hat{q}_Y\,\mathbf{e}_Y \tag{4b}$$

and $(\mathbf{e}_X, \mathbf{e}_Y, \mathbf{e}_Z)$ denotes the Cartesian basis. We have assumed that the in-plane projection of $\hat{\mathbf{u}}$ scales like η, that its out-of-plane projection $\hat{w}$ is independent of η, and that both components of $\hat{\mathbf{q}}$ scale like η^2. As we shall see, these scaling assumptions allow the various contributions entering in the strain measures to

be balanced. They are moreover natural in the context of the vertex model, and are similar to the scaling assumptions underlying the classical theory of plates, see for instance [3].

S1.2 Expansion of the energy of a single cell

The energy (1) can be rewritten as a sum over all cells of an energy per cell, $\mathcal{E}_{\rm vm} = \sum_f \epsilon_f$, where

$$\epsilon_f = \frac{1}{2}(A_f - 1)^2 + \frac{G}{2}\, P_f + \frac{H}{2} {P_f}^2 + \frac{B}{2} \sum_{\langle f, f' \rangle} (1 - \mathbf{N}_f \cdot \mathbf{N}_{f'}). \tag{5}$$

On the right-hand side, the sum runs over all faces f' adjacent to f. Note the division by 2 in the G and B terms, which comes from the fact that a given edge belongs to two faces, and is therefore counted twice when summing over all faces.

To homogenize the vertex model, we consider the energy $\epsilon_{f=0}$ of the face $f = 0$ centered at the origin $(X, Y) = (0, 0)$ in the limit $\eta \to 0$, and derive an asymptotic expression of $\epsilon_{f=0}$ as a function of the rescaled wavevector $\mathbf{K}$, of the rescaled complex in-plane displacement $\hat{\mathbf{v}}$ and of the complex out-of-plane displacement $\hat{w}$.

In reference configuration, the vertices $\mathbf{X}_j$ of the face $f = 0$ are

$$\mathbf{X}_j = L^0\, (\cos\theta_j, \sin\theta_j, 0)$$

where $1 \leq j \leq 6$ is an integer and $\theta_j = (2\,j + 1)\,\frac{\pi}{6}$; the reference position of the vertices of the adjacent cells are calculated similarly. Using equations (3–4), one can calculate the position $\mathbf{x}_j$ of all vertices belonging to the central cells and to its adjacent cells in actual configuration as a function of j, a, η, $\mathbf{K}$, $\hat{\mathbf{v}}$, $\hat{\mathbf{q}}$, $\hat{w}$ and $\hat{s}$. One can then calculate all the quantities entering in the definition of the energy as follows (see main text for their definition): one expresses the area vector $\mathbf{A}_f$, the scalar area A_f and the unit normal $\mathbf{N}_f$ for the central cell $f = 0$ and its adjacent cells. Inserting into equation (5), we obtain the expression of the energy of the face $f = 0$, $\epsilon_{f=0}(a, \eta, \mathbf{K}, \hat{\mathbf{v}}, \hat{\mathbf{q}}, \hat{w}, \hat{s})$.

Next, we expand this expression of $\epsilon_{f=0}$ in a series with respect to η up to fourth order. Doing this calculation by hand is tedious. We carried it out using the symbolic calculation language Wolfram Mathematica [8]. The result is

$$\begin{aligned}
\epsilon_{f=0}(a, \eta, \mathbf{K}, \hat{\mathbf{v}}, \hat{\mathbf{q}}, \hat{w}, \hat{s}) = \epsilon_{\rm PE}(a) &+ \frac{\epsilon'_{\rm PE}(a)}{2\,a} \left\{ - a\, \mathbf{K} \cdot \mathbf{v}_{\rm im} + \frac{1}{2}\, |\mathbf{K}|^2\, w_{\rm im}^2 \right\} \eta^2 \cdots \\
&+ \left\{ \frac{\epsilon'_{\rm PE}(a)}{24\,\sqrt{3}} \left[|\mathbf{K}|^2\, \mathbf{K} \cdot \mathbf{v}_{\rm im} - \frac{|\mathbf{K}|^4}{a}\, w_{\rm im}^2 + \frac{3^{3/4}}{\sqrt{2}}\, \mathbf{q}_{\rm re} \cdot \mathcal{S} : (\mathbf{K} \otimes \mathbf{K}) \right] + \frac{2\,a^2 - \tilde{G}}{4}\, (\mathbf{K} \cdot \mathbf{v}_{\rm im})^2 \cdots \right. \\
&+ \left(\frac{1}{4}\, \tilde{G} + \sqrt{3}\, H \right) \left[\frac{3}{2}\, |\mathbf{K}|^2\, |\mathbf{v}_{\rm im}|^2 + 3\,\sqrt{3}\, (|\mathbf{q}_{\rm re}|^2 + 2\, s_{\rm re}^2) + \sqrt{2}\, 3^{3/4}\, \mathbf{q}_{\rm re} \cdot \mathcal{S} : \left(\mathbf{K} \otimes \left(\mathbf{v}_{\rm im} - \frac{w_{\rm im}^2}{2\,a}\, \mathbf{K} \right) \right) \right] \cdots \\
&+ \frac{1 - \frac{3}{4}\, \tilde{G} - \sqrt{3}\, H}{8\, a^2}\ \left(-4\, a\, |\mathbf{K}|^2\, \mathbf{K} \cdot \mathbf{v}_{\rm im}\, w_{\rm im}^2 + |\mathbf{K}|^4\, w_{\rm im}^4 \right) + \frac{\frac{1}{4}\, \tilde{G} + \sqrt{3}\, H + 6\, \frac{B}{a^2}}{4\,\sqrt{3}}\, |\mathbf{K}|^4\, w_{\rm re}^2 \left. \right\} \eta^4 + \mathcal{O}(\eta^6)
\end{aligned} \tag{6}$$

where $\mathbf{v}_{\rm im} = \Im(\hat{\mathbf{v}})$, $w_{\rm im} = \Im(\hat{w})$ (the subscript 'im' and the operator $\Im$ denote the imaginary part), $\mathbf{q}_{\rm re} = \Re(\hat{\mathbf{q}})$, $w_{\rm re} = \Re(\hat{w})$, $s_{\rm re} = \Re(\hat{s})$ (the subscript 're' and the operator $\Re$ denote the real part), $\tilde{G}$ is a shorthand for

$$\tilde{G} = \frac{\sqrt[4]{3}\, G}{\sqrt{2}\, a}, \tag{7}$$

and the constant term $\epsilon_{\rm PE}(a)$ denotes the energy of the intermediate configuration 'PE' (uniform scaling transformation with ratio a):

$$\epsilon_{\rm PE}(a) = \frac{1}{2}\, (1 - a^2)^2 + a^2\, (2\,\tilde{G} + 4\,\sqrt{3}\, H), \tag{8}$$

see also equation (6) in the main text.

In equation (6), we have also introduced a tensor of rank 3 living in the tangent plane (X, Y). It is defined in terms of the matrices $\mathbf{S}_X$ and $\mathbf{S}_Y$ obtained by fixing the first index: $\mathcal{S} = \mathbf{e}_X \otimes \mathbf{S}_X + \mathbf{e}_Y \otimes \mathbf{S}_Y$ where

$$\mathbf{S}_X = \begin{pmatrix} \mathcal{S}_{XXX} & \mathcal{S}_{XXY} \\ \mathcal{S}_{XYX} & \mathcal{S}_{XYY} \end{pmatrix} = \begin{pmatrix} 0 & 1 \\ 1 & 0 \end{pmatrix} \quad \text{and} \quad \mathcal{S}_Y = \begin{pmatrix} \mathcal{S}_{YXX} & \mathcal{S}_{YXY} \\ \mathcal{S}_{YYX} & \mathcal{S}_{YYY} \end{pmatrix} = \begin{pmatrix} 1 & 0 \\ 0 & -1 \end{pmatrix} \tag{9}$$

We shall refer to $\mathbf{S}_X$ and $\mathbf{S}_Y$ as the *spin matrices*. Note that these matrices are symmetric, and such that $\mathbf{S}_X^2 = \mathbf{S}_Y^2 = \mathbf{I}_2$ where $\mathbf{I}_2$ is the identity matrix in dimension 2. In equation (6), the triple contraction of $\mathcal{S}$ is defined by

$$\mathbf{q}_{\rm re} \cdot \mathcal{S} : \mathbf{A} = \sum_{i,j,k \in \{X,Y\}} q^i_{\rm re} \mathcal{S}_{ijk} A_{jk} = q^X_{\rm re}\, \mathbf{S}_X : \mathbf{A} + q^Y_{\rm re}\, \mathbf{S}_Y : \mathbf{A} \tag{10}$$

where $q^i_{\rm re}$, $\mathcal{S}_{ijk}$, and A_{jk} denote the components of the vector $\mathbf{q}_{\rm re}$, of the tensor $\mathcal{S}$ and of the matrix $\mathbf{A}$ in the Cartesian basis $(\mathbf{e}_X, \mathbf{e}_Y)$, respectively. Since $\mathcal{S}$ is symmetric with respect to its last two indices, the pairing of indices in the double contraction on the right-hand side is unimportant.

Note that the right-hand side of equation (6) involves only scalar invariants built from the vectors $\mathbf{K}$, $\mathbf{v}_{\rm im}$ and $\mathbf{q}_{\rm re}$, and from the tensor $\mathcal{S}$.

S1.3 Macroscopic strain measures

Our goal is now to identify the strain quantities relevant to the theory of thin plates, namely the stretching strain and the mean curvature, in the right-hand side of equation (6). We start by the macroscopic stretching strain. Let us first define the macroscopic displacement $\mathbf{x}_{\rm macro}$, obtained by averaging out the microscopic displacement from equation (3):

$$\mathbf{x}_{\rm macro} = a\, \mathbf{X} + \Re\left(\hat{\mathbf{u}}\, e^{i\,\eta\, \mathbf{K}\cdot\mathbf{X}}\right) \tag{11}$$

The corresponding deformation gradient reads

$$\mathbf{F}_{\rm macro} = \frac{\partial \mathbf{x}_{\rm macro}}{\partial \mathbf{X}}. \tag{12}$$

The stretching strain is given by the (macroscopic) Cauchy-Green tensor $\mathbf{E}$ which we define by

$$\mathbf{E} = \frac{1}{2\,a}\left(\mathbf{F}^T_{\rm macro} \cdot \mathbf{F}_{\rm macro} - a^2\, \mathbf{I}_2\right). \tag{13}$$

This definition is such that $\mathbf{E} = \mathbf{0}$ in the intermediate configuration 'I'. The prefactor $1/(2\,a)$ warrants that that $\operatorname{tr} \mathbf{E}$ can be interpreted as the relative increase of area from the intermediate configuration, in the linear case (see below). Note that the dimension of $\mathbf{E}$ is 2×2.

To gain some insight into the Cauchy-Green tensor, we derive its explicit expression when the incremental macroscopic displacement (v_X, v_Y, w) is a generic function, *i.e.* when the final position is $\mathbf{x}_{\rm macro} = a\,\mathbf{X} + v_X(\mathbf{X})\,\mathbf{e}_X + v_Y(\mathbf{X})\,\mathbf{e}_Y + w(\mathbf{X})\,\mathbf{e}_Z$. Inserting into equation (13), we find

$$E_{ij} = \frac{v_{j,i} + v_{i,j}}{2} + \frac{1}{2\,a}\, v_{k,i}\, v_{k,j} + \frac{1}{2\,a}\, w_{,i}\, w_{,j}, \tag{14}$$

where indices (i, j, k) run over the in-plane directions X and Y, a comma in subscript stands for a partial derivative, and we use the Einstein summation convention. The first term on the right-hand side is the linear strain, the second term can be neglected in buckling analysis (the Föppl-von Kàrmàn approximation of the strain) and the last non-linear term couples stretching with the deflection w.

Returning to the special Fourier form (3) of the displacement and to our scaling assumption (4), we write the macroscopic deformation gradient at the origin $(X, Y) = (0, 0)$ as

$$\mathbf{F}_{\rm macro}(0,0) = \left.\frac{\partial \mathbf{x}_{\rm macro}}{\partial \mathbf{X}}\right|_{\mathbf{X}=\mathbf{0}} = a\,\mathbf{I}_{3\times 2} + \Re(\hat{\mathbf{u}} \otimes i\,\eta\,\mathbf{K}) = a\,\mathbf{I}_{3\times 2} - (\eta\,\mathbf{v}_{\rm im} + w_{\rm im}\,\mathbf{e}_Z) \otimes \eta\,\mathbf{K}, \tag{15}$$

where $\mathbf{I}_{3\times 2}$ is the matrix of size 3×2 obtained by appending a zero row at the bottom of the identity matrix $\mathbf{I}_2$, and $\otimes$ denotes the outer product of vectors.

The corresponding macroscopic Cauchy-Green strain tensor reads, by equation (13),

$$\mathbf{E}(0,0) = -\eta\,\mathbf{v}_{\rm im}\odot\eta\,\mathbf{K} + \frac{\eta\,\mathbf{K}\otimes\eta\mathbf{K}}{2\,a}\,(\eta^2\,|\mathbf{v}_{\rm im}|^2 + w_{\rm im}^2), \tag{16}$$

where $\mathbf{a}\odot\mathbf{b} = \frac{\mathbf{a}\otimes\mathbf{b}+\mathbf{b}\otimes\mathbf{a}}{2}$ denotes the symmetrized outer product. This equation is a variant of equation (14) in tensor notation.

We now proceed to calculate the mean curvature. We denote by Δ the Laplacian operator with respect to the reference coordinates (X,Y), $\Delta = \frac{\partial^2}{\partial X^2} + \frac{\partial^2}{\partial Y^2}$. The mean curvature is given in terms of the Laplacian of the deflection $\mathbf{x}_{\rm macro}\cdot\mathbf{e}_Z = \Re(\hat{w}\,e^{i\,\eta\,\mathbf{K}\cdot\mathbf{X}})$ as

$$\frac{1}{2\,a^2}\,\Delta w(0,0) = \frac{1}{2\,a^2}\,\Delta[\Re(\hat{w}\,e^{i\,\eta\,\mathbf{K}\cdot\mathbf{X}})]_{\mathbf{X}=\mathbf{0}} = -\frac{1}{2\,a^2}\,|\eta\,\mathbf{K}|^2\,w_{\rm re}. \tag{17}$$

The coefficient a^2 in the denominator converts the Laplacian Δ with respect to the Lagrangian coordinates, to a Laplacian with respect to the coordinates in the intermediate configuration 'PE'.

We now proceed to rewrite the expansion (6) in terms of the Cauchy-Green strain and the mean curvature, see equations (16–17).

S1.4 Stretch in intermediate configuration

We observe that the η^2 term in the expansion (6) involves the trace of the Cauchy-Green tensor:

$$\epsilon_{f=0}(a,\eta,\mathbf{K},\hat{\mathbf{v}},\hat{\mathbf{q}},\hat{w},\hat{s}) = \epsilon_{\rm PE}(a) + \epsilon'_{\rm PE}(a)\,\frac{\operatorname{tr}\mathbf{E}(0,0)}{2} + \mathcal{O}(\eta^4), \tag{18}$$

where $\mathbf{E}(0,0) = \mathcal{O}(\eta^2)$. This term cancels by the condition

$$\epsilon'_{\rm PE}(a) = 0. \tag{19}$$

This expression defines (implicitly) the stretch a in the intermediate configuration making the energy stationary, *i.e.* relaxing the in-plane stretch.

To derive the plate model, we will need to analyze the next order in the expansion, η^4.

S1.5 Continuous energy as a function of microscopic shift

We can now simplify the energy of the vertex model in equation (6) in two ways: we use the implicit equation (19) for a, which allows to get rid of the two terms proportional to $\epsilon'_{\rm PE}(a)$, and we rewrite the remaining terms using the macroscopic Cauchy-Green tensor $\mathbf{E}(0,0)$ and the mean curvature calculated in §S1.3.

With the help of the symbolic calculation language Wolfram Mathematica (see the companion notebook for details), we find

$$\begin{aligned}\epsilon_{f=0}(a,\eta,\mathbf{K},\hat{\mathbf{v}},\hat{\mathbf{q}},\hat{w},\hat{s}) = \epsilon_{\rm PE}(a) + \frac{\lambda_*}{2}\,\operatorname{tr}^2\mathbf{E}(0,0) + \mu_*\,|\mathbf{E}(0,0)|^2 + \frac{\beta}{2}\,\big(\Delta w(0,0)\big)^2\cdots\\ + \frac{\tau}{2}\,\eta^4\,\big(|\mathbf{q}(0,0)|^2 + 2\,s^2(0,0)\big) - \gamma\,\eta^2\,\mathbf{q}(0)\cdot\mathcal{S}:\mathbf{E}(0,0) + \mathcal{O}(\eta^6)\end{aligned} \tag{20}$$

where $|\mathbf{E}^2| = \mathbf{E}:\mathbf{E} = \operatorname{tr}(\mathbf{E}\cdot\mathbf{E})$, and $\mathbf{q}(0,0)$ and $s(0,0)$ denote the scaled tangent and normal components of the microscopic displacement at the origin, $\mathbf{q}(0,0) = \Re(\hat{\mathbf{q}}) = \mathbf{q}_{\rm re}$ and $s(0,0) = \Re(\hat{s}) = s_{\rm re}$. The moduli are

found by this identification as

$$\lambda_* = 1 - \frac{9}{4}\,(1 - a^2) + 2\,\sqrt{3}\,H \tag{21a}$$

$$\mu_* = \frac{3}{4}\,(1 - a^2) \tag{21b}$$

$$\beta = \frac{1 - a^2}{8\,\sqrt{3}} + \frac{\sqrt{3}}{a^2}\,B \tag{21c}$$

$$\tau = \frac{3\,\sqrt{3}}{2}(1 - a^2) \tag{21d}$$

$$\gamma = \frac{3^{3/4}}{2\,\sqrt{2}}\,(1 - a^2). \tag{21e}$$

The first line in equation (20) defines a smooth plate model, compare with equation (2). However, we must take care of the other terms involving the microscopic displacement (see below) before we can derive the equivalent plate model.

Note that $\mathbf{E}(0,0)$ and $\Delta w(0,0)$ are quantities of order η^2, see equations (16) and (17): except for the constant term $\epsilon_{\mathrm{PE}}(a)$, all terms on the right-hand side of equation (20) are of order η^4. This justifies the scaling assumptions proposed in §S1.1.

Note that both sides of equation (20) are evaluated at the central cell, $f = 0$, which, in the continuous description, is used as the origin of the axes $(X, Y) = (0, 0)$; this is consistent.

S1.6 Relaxed continuous energy

The microscopic shift $\mathbf{p}(0,0) = \eta^2\,(\mathbf{q}(0,0) + s(0,0)\,\mathbf{e}_Z)$ between the two Bravais sublattices is found by minimizing the continuous energy appearing on the right-hand side of equation (20). We observe that $s(0,0)$ appears only in the form $s^2(0,0)$ in the τ-term. This term is minimum for

$$s(0,0) = 0, \tag{22}$$

and we conclude that the microscopic shift vector is in-plane.

The scaled in-plane component $\mathbf{q}$ of the microscopic shift $\mathbf{p}$ appears in the two last terms of equation (20). The stationarity condition of this right-hand side reads $\tau\,\eta^4\,\mathbf{q}(0,0) - \gamma\,\eta^2\,\mathcal{S} : \mathbf{E}(0,0)$. Therefore, the microscopic shift reads

$$\mathbf{p}(0,0) = \eta^2\,\mathbf{q}(0,0) = \frac{\gamma}{\tau}\,\mathcal{S} : \mathbf{E}(0,0), \tag{23}$$

where the tensor $\mathcal{S}$, of rank 3, has been defined in equation (9). This important relation yields the microscopic shift $\mathbf{p}$ in terms of the macroscopic Cauchy-Green tensor $\mathbf{E}$. It has been established for the central cell $f = 0$ lying at the origin of the coordinate system $(X, Y) = (0, 0)$ but is obviously valid everywhere. Therefore we drop the coordinates $(0, 0)$.

Inserting this optimal value of the shift $\mathbf{q}$ into the energy terms written on the second line of equation (20), we have

$$\frac{\tau}{2}\,\eta^4\,\left(|\mathbf{q}|^2 + 2\,s^2\right) - \gamma\,\eta^2\,\mathbf{q}\cdot\mathcal{S} : \mathbf{E} = \frac{\tau}{2}\,|\mathbf{p}|^2 - \gamma\,\mathbf{p}\cdot\mathcal{S} : \mathbf{E} = -\frac{\gamma^2}{2\,\tau}\,\left(\mathcal{S} : \mathbf{E}\right)^2$$

This expression can be further simplified by using the expressions for τ and γ in equation (21) and the identity $(\mathcal{S} : \mathbf{E})^2 = -\,\mathrm{tr}^2\,\mathbf{E} + 2\,|\mathbf{E}|^2$ (which can easily be established for any symmetric matrix $\mathbf{E}$ using the definition of the tensor $\mathcal{S}$):

$$\frac{\tau}{2}\,\eta^4\,\left(|\mathbf{q}|^2 + 2\,s^2\right) - \gamma\,\eta^2\,\mathbf{q}\cdot\mathcal{S} : \mathbf{E} = \frac{1 - a^2}{4}\,\left(\frac{\mathrm{tr}^2\,\mathbf{E}}{2} - |\mathbf{E}|^2\right) \tag{24}$$

Inserting this into the right-hand side of equation (20), we find the relaxed energy as

$$\epsilon_{f=0}^{\mathrm{relaxed}}(a, \eta, \mathbf{K}, \hat{\mathbf{v}}, \hat{w}) = \epsilon_{\mathrm{PE}}(a) + \frac{\lambda}{2}\,\mathrm{tr}^2\,\mathbf{E}(0,0) + \mu\,|\mathbf{E}(0,0)|^2 + \frac{\beta}{2}\,\left(\Delta w(0,0)\right)^2 + \mathcal{O}(\eta^6) \tag{25}$$

where the new elastic moduli effectively capture the microscopic field,

$$\lambda = \lambda_* + \frac{1-a^2}{4} = -1 + 2\,a^2 + 2\,\sqrt{3}\,H \tag{26a}$$

$$\mu = \mu_* - \frac{1-a^2}{4} = \frac{1}{2}\,(1-a^2) \tag{26b}$$

$$\beta = \qquad\qquad \frac{1-a^2}{8\,\sqrt{3}} + \frac{\sqrt{3}}{a^2}\,B. \tag{26c}$$

Here, λ and μ are Lamé parameters for stretching (μ is a shear modulus), and β is the bending modulus.

Summing equation (25) over all cells, we obtain the total energy of the vertex model on the left-hand side, and the energy of a continuous plate model on the right-hand side,

$$\mathcal{E}_{\rm vm} = \mathcal{E}_{\rm plate} + A\,\epsilon_{\rm PE}(a) + \mathcal{O}(\eta^6), \tag{27}$$

where $A = \iint \mathrm{d}X\,\mathrm{d}Y$ is the undeformed domain area. Note that all cells have a unit area in reference configuration and, as a result, a sum over cells is equivalent in the smooth limit to an integral over the reference domain.

Equation (27) establishes the asymptotic equivalence of the discrete vertex model and of the continuous plate model for any long-wavelength harmonic perturbation (up to an unimportant constant term). By the principle of linear superposition, the equivalence between these linear models holds for an arbitrary long-wavelength perturbation. At this order in the expansion, the hexagonal lattice is effectively isotropic.

S1.7 Material stability

In 2D, the thermodynamic stability requires that the Lamé parameters λ and μ appearing in the stretching term in equation (26a–26b) satisfy $\mu > 0$ and $\lambda + \mu \geq 0$: $\mu = 0$ corresponds to the minimum possible Poisson's ratio $\nu = -1$, while $\lambda + \mu = 0$ corresponds to its maximum $\nu = 1$ (area-preserving material in 2D). For a fixed value of (G, H), only the roots a of equation (19) satisfying these conditions must be considered — if they exist. For a thorough discussion of stability of hexagonal solutions of the vertex model, see [6]. In the case $H = 0$ considered in our numerical study, Eq. (7) of the main text reads $\tilde{G} = 1 - a^2$ when expressed in terms of the quantity $\tilde{G}$ defined above in equation (7): the two stability conditions, $\mu > 0$ and $\lambda + \mu \geq 0$, correspond to $1/\sqrt{3} \leq a < 1$, *i.e.* $0 < G < 2^{3/2}/3^{7/4} \approx 0.4136$.

S1.8 Comparison to the moduli derived by Staple et al.

Our expressions in Eq. 7 of the main text correct those derived by Staple et al. [6], as we explain here.

The equation 15 in [6], gives what the authors call a *shear modulus* $\overline{\mu}$ and a *compression modulus* $\overline{\lambda}$. When converted to our notation, they read $\overline{\mu} = \lambda + \mu$ and $\overline{\lambda} = 2\,\mu$. These expressions need to be corrected as follows. Their moduli have been mixed up: $\overline{\lambda}$ is actually proportional to the shear modulus μ (and not to the compression modulus) and $\overline{\mu}$ to the bulk modulus $K = \lambda + \mu$ (and not to the shear modulus). Their shear modulus $\overline{\lambda}$ is off by an extra factor 2, an error that can be traced back to their equation 13: on the right-hand side of this equation, the factor 1/2 should read 1/4. With these corrections, their moduli agree with our λ_* and μ_* appearing in equations (21a–21b).

Still, these moduli are unphysical, as they ignore the microscopic shift vector $\mathbf{p}$ between the two sublattices (also known as *inner elasticity*). The physical moduli are those given above in equation (26a–26c).

S2 Detailed calculation of the pre-stress in the planar solution

We start by considering planar solutions, assuming that $w(R)$ is identically zero. The only unknown is the radial displacement $v(R)$. The Cauchy-Green tensor is given in the main text as

$$E_R = v'(R) + \frac{w'^2(R)}{2} \tag{28a}$$

$$E_\Theta = \frac{v(R)}{R}. \tag{28b}$$

The membrane stress tensor $\mathbf{S}$ has the same symmetry , and its eigenvalues S_R and S_Θ are given by the linear constitutive law associated with the quadratic stretching energy, $\mathbf{S} = \lambda\,\mathrm{tr}(\mathbf{E})\,\mathbf{I}_2 + 2\,\mu\,\mathbf{E}$:

$$\begin{pmatrix} S_R \\ S_\Theta \end{pmatrix} = \begin{pmatrix} 2\,\mu + \lambda & \lambda \\ \lambda & 2\,\mu + \lambda \end{pmatrix} \cdot \begin{pmatrix} E_R \\ E_\Theta \end{pmatrix}. \tag{29}$$

Combining the definition of the strain in equation (28b), the constitutive law (29) and the equation of equilibrium $\frac{1}{R}\frac{\mathrm{d}}{\mathrm{d}R}(R\,S_R) - \frac{S_\Theta}{R} = 0$, we find the equation $-\frac{v}{R} + v' + R\,v'' = 0$ whose solutions are linear combinations of the function R and $1/R$. Let us denote by $[\![f]\!]$ the jump $[\![f]\!] = f(R_1^+) - f(R_1^-)$ of a function f across the contractile circle at $R = R_1$. The solutions $v(R)$ of the differential equation which satisfy the condition at the center $v(0) = 0$, the clamping condition $v(R_2) = 0$ and the continuity at the contractile ring $[\![v]\!]_{R_1} = 0$ can be expressed in terms a single unknown amplitude $C = v(R_1)$ as

$$v(R) = \begin{cases} C\,\frac{R}{R_1} & \text{if } R < R_1 \\ \frac{C}{R_1\,(1-\alpha^2)}\,\left(R - \frac{R_2^2}{R}\right) & \text{if } R_1 < R < R_2, \end{cases} \tag{30}$$

where α denotes the radius of the domain relative to that of the contractile ring,

$$\alpha = \frac{R_2}{R_1}. \tag{31}$$

To find the parameter C, one can either minimize the total energy of the problem or use the balance of stress across the contractile ring (2D Young-Laplace equation):

$$[\![S_R]\!] - \frac{\Gamma}{R_1} = 0. \tag{32}$$

Both methods yield the same result, $C = -\frac{\alpha^2-1}{2\,\alpha^2}\,\frac{\Gamma}{\lambda+2\,\mu}$. In terms of Poisson's ratio $\nu = \frac{1}{1+\frac{2\,\mu}{\lambda}}$, this yields

$$C = -\frac{\alpha^2 - 1}{2\,\alpha^2}\,\frac{\nu\,\Gamma}{\lambda} \tag{33}$$

The corresponding stress can then be found from the constitutive law as

$$S_R = \begin{cases} -\frac{1+\nu}{2}\,S^* & \text{if } R < R_1 \\ \frac{S^*}{\alpha^2-1}\,\left(\frac{1+\nu}{2} + \frac{1-\nu}{2}\,\frac{\alpha^2}{(R/R_1)^2}\right) & \text{if } R_1 < R < R_2. \end{cases} \tag{34a}$$

$$S_\Theta = \begin{cases} -\frac{1+\nu}{2}\,S^* & \text{if } R < R_1 \\ \frac{S^*}{\alpha^2-1}\,\left(\frac{1+\nu}{2} - \frac{1-\nu}{2}\,\frac{\alpha^2}{(R/R_1)^2}\right) & \text{if } R_1 < R < R_2, \end{cases} \tag{34b}$$

where we have introduced the typical membrane stress S^*,

$$S^* = \frac{\alpha^2 - 1}{\alpha^2}\,\frac{\Gamma}{R_1}. \tag{35}$$

The stress in equation (34) is relevant to the planar (unbuckled) configuration. The planar configuration serves as the base solution of the forthcoming stability analysis, and in this context the stress will be referred to as *pre-stress*. The pre-stress is compressive in the interior region $R < R_1$, as $S_R = S_\Theta < 0$ there, and tensile in the outer region.

The pre-stress in equation (34) takes a particularly simple form in the limit $\nu = 1$ where the membrane preserves area (2D 'incompressibility', $\mu \ll \lambda$): then the stress is piecewise constant and isotropic,

$$S_R(R) = S_\Theta(R) = -S^*\, t(R) \tag{36}$$

where $t(R)$ is the piecewise function

$$t(R) = \begin{cases} 1 & \text{if } R < R_1 \\ -\frac{1}{\alpha^2-1} & \text{if } R_1 < R < R_2. \end{cases} \tag{37}$$

S3 Stability analysis of the axisymmetric plate

We solve the equations for the linear stability of a circular plate in axisymmetric geometry, driven by the contraction Γ of the embedded circle. The pre-stress is locally isotropic and piecewise constant, and writes $\mathbf{S} = -S^*\, t(R)\, \mathbf{I}_2$, where S^* is a typical stress defined in the main text. The classical equation for the linear stability of a circular plate [5, 7] has been recalled in the main text. In dimensionless form, it reads

$$-\frac{1}{\overline{R}}\,\frac{\mathrm{d}(\overline{R}\,q'(\overline{R}))}{\mathrm{d}\overline{R}} + \frac{q(\overline{R})}{\overline{R}^2} - \gamma\,\bar{t}(\overline{R})\,q(\overline{R}) = 0, \tag{38}$$

where $\overline{R} = R/R_1$ is the dimensionless radial coordinate which varies in the domain $0 < \overline{R} < \alpha$, the upper bound being the geometrical parameter $\alpha = \frac{R_2}{R_1}$, the quantity $q(\overline{R})$ is the radial slope, γ is the dimensionless buckling parameter defined in the main text as $\gamma = \frac{\Gamma R_1}{\beta}\,\frac{\alpha^2-1}{\alpha^2}$, and $\bar{t}(\overline{R})$ is the dimensionless form of the piecewise constant function entering in the distribution of pre-stress,

$$\bar{t}(\overline{R}) = \begin{cases} 1 & \text{if } 0 < \overline{R} < 1 \\ -\frac{1}{\alpha^2-1} & \text{if } 1 < \overline{R} < \alpha \end{cases}.$$

According to the method of linear stability analysis, the instability threshold $\gamma_\mathrm{c}(\alpha)$ is detected by the existence of a non-trivial solution $q(\overline{R})$ to equation (38) with the following boundary conditions: $q(0) = 0$ enforces the continuity of the slope at the center $\overline{R} = 0$, and $q(\alpha) = 0$ enforces the clamp condition on the outer boundary. This clamp condition assumes that the rotation is blocked along the outer boundary in the continuous model, and can be justified as follows. In the simulation of the vertex model, we use a *simple support* condition along the outer hexagonal boundary, *i.e.* we block the *position* of the outer set of vertices but let free the *rotation* of the adjacent edges. We observe that this *simple support* condition is equivalent to a *clamping* condition in the *axisymmetric* problem. Indeed, a finite slope $q(\alpha)$ on the circular edge of the perfectly axisymmetric plate implies a significant amount of stretching in the vertex model with hexagonal symmetry, especially near the corners of the hexagonal boundary. This stretching is zero when averaging over the azimuthal direction but is still associated with a high cost in elastic energy. For this reason, the rotation at the outer edge is effectively blocked. We have checked that the buckling modes of the vertex model indeed have a very small slope $q(\alpha)$ on the outer edge (after averaging in the azimuthal direction), as seen in the comparison of the mode shapes in figure 3C of the main text.

In both of the inner and outer regions $0 < \overline{R} < 1$ and $1 < \overline{R} < \alpha$, the dimensionless pre-stress $\gamma\,\bar{t}$ in equation (38) is constant and the generic solution q can be expressed as a combination of the Bessel function of the first kind J_1 and of the second kind, Y_1, as

$$\begin{aligned} q(\overline{R}) &= \mathcal{A}\, J_1\left(\sqrt{\gamma}\,\overline{R}\right) && \text{for } 0 < \overline{R} < 1 \\ q(\overline{R}) &= \mathcal{B}\, J_1\left(i\,\frac{\sqrt{\gamma}}{\sqrt{\alpha^2-1}}\,\overline{R}\right) + \mathcal{C}\, Y_1\left(i\,\frac{\sqrt{\gamma}}{\sqrt{\alpha^2-1}}\,\overline{R}\right) && \text{for } 1 < \overline{R} < \alpha. \end{aligned} \tag{39}$$

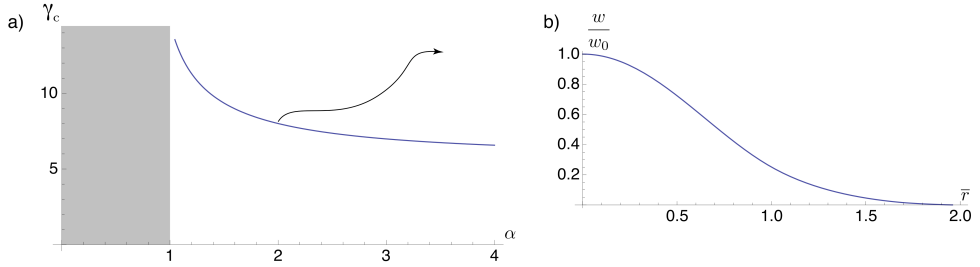

Figure S2: Linear stability analysis of an axisymmetric plate. (a) Dimensionless instability threshold γ_c as a function of the aspect-ratio α. (b) Normalized deflection of the buckling mode for $\alpha = 2$. The deflection w is reconstructed by integrating the slope q along the radial direction, $w(\overline{R}) \propto \int_0^{\overline{R}} q(\overline{R}')\,\mathrm{d}\overline{R}'$.

To avoid a singularity for $\overline{R} \to 0$, the coefficient of the function Y_1 that is divergent near zero has been set to zero in the inner region $0 < \overline{R} < 1$.

The constants $\mathcal{A}$, $\mathcal{B}$ and $\mathcal{C}$ are found from the conditions of continuity at $\overline{R} = 1$, and from the clamping condition $q(\alpha) = 0$,

$$q(1^-) = q(1^+) \tag{40a}$$
$$q'(1^-) = q'(1^+) \tag{40b}$$
$$q(\alpha) = 0 \tag{40c}$$

Here, equation (40a) warrants continuity of the radial slope $q \propto w'$ at the contractile circle and equation (40b) expresses the balance of moments across this contractile circle — note that the curvature q' in the radial direction is proportional to the internal moment. When above solutions for q are inserted, this yields a set of linear equations for the unknown coefficients

$$\mathbf{M}(\alpha, \gamma) \cdot \begin{pmatrix} \mathcal{A} \\ \mathcal{B} \\ \mathcal{C} \end{pmatrix} = \mathbf{0},$$

where the coefficients of the 3×3 matrix $\mathbf{M}(\alpha, \gamma)$ involve Bessel's functions and their derivatives. The buckling threshold is then given by the implicit equation

$$\det \mathbf{M}(\alpha, \gamma_c(\alpha)) = 0,$$

connecting α and γ. This equation is solved graphically in Fig. S2.

S4 Dependence of the buckling threshold on the bending modulus B

In figure S3, we show the dependence of the buckling threshold Γ_c on the bending modulus B for $(G, H) = (0.03514, 0)$, and for different geometries of the vertex model (symbols) having a constant ratio $P_2/P_1 = 2$, hence $\alpha \approx 2$. Datapoints nearly collapse onto the line plotted using Eq. [13] of the main text, featuring the typical values $\alpha = \frac{R_2}{R_1} = \frac{13.2}{6.9} = 1.91$ and $R_1 = 6.9$ from the vertex model. In the continuous model, we use linearized effective moduli since G is small and $H = 0$.

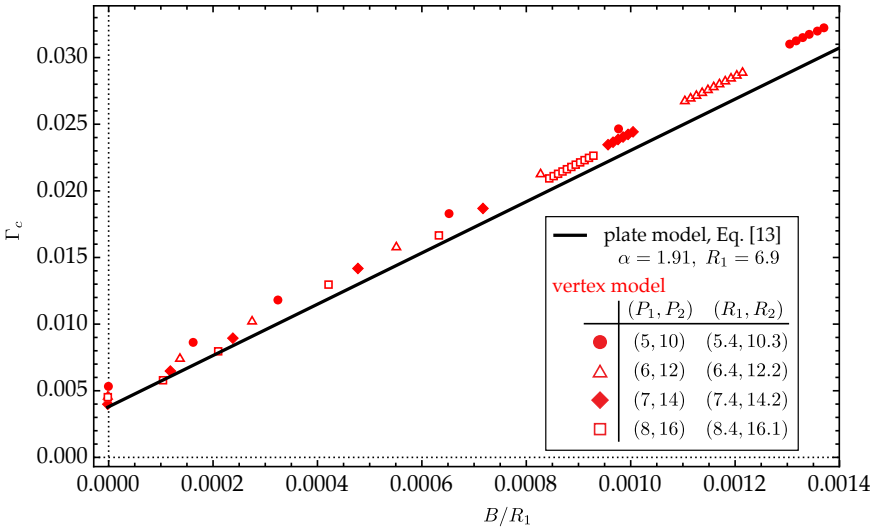

Figure S3: The buckling threshold Γ_c as a function of the bending modulus B, for $(G, H) = (0.03514, 0)$: comparison of the predictions of the vertex model for different geometries such that $P_2/P_1 = 2$, and of the continuous plate model. In the plate model, we use the linearized effective moduli $\beta_{\rm lin}$. The existence of a *residual* bending modulus is apparent from the fact that the threshold Γ_c is non-zero when $B = 0$. This residual bending modulus is accurately captured by the plate model, *i.e.* the black line does not pass through the origin.

S5 Comparison of the strain and stress maps: vertex model versus plate model

Here, we visualize the in-plane strain and stress corresponding to an equilibrium solution of the discrete vertex model, and compare them to the predictions of the continuous plate model.

To compute the strain $\mathbf{E}$ in a hexagonal mesh obtained from numerical simulations, we triangulate the mesh and calculate a constant strain on each triangle using the classical *constant strain element* (CST). Next, we evaluate its components $E_{RR} = \mathbf{e}_R \cdot \mathbf{E} \cdot \mathbf{e}_R$, $E_{\Theta\Theta} = \mathbf{e}_\Theta \cdot \mathbf{E} \cdot \mathbf{e}_\Theta$ and $E_{R\Theta} = \mathbf{e}_R \cdot \mathbf{E} \cdot \mathbf{e}_\Theta$ in the polar basis. In figure S4, the strain map is shown for $P_1 = 8$ internal layers (corresponding to $n_1 = 217$ cells inside the contractile hexagon), $P_2 = 16$ layers (corresponding to a total number of cells $n_2 = 817$), $G = 0.0351$, $H = 0$ (no perimeter term) and $\Gamma = 0.0217$. The discrete bending modulus B is set to $B = 0.00738$ such that this planar configuration is stable but very close to the buckling threshold.

The resulting strain is highly non-axisymmetric, as shown in Fig. S4. There is a large concentration of strain near the corners of the contractile hexagons – linear elasticity indeed predicts that the strain and stress diverge near these corners.

Averaging the strain and stress in the azimuthal direction Θ, one obtains much smoother profiles, see Fig. S5. As predicted by the smooth model, the averaged membrane stress is isotropic and homogeneous far from the contracting circle, both near the center and near the outer boundary. The values of this homogeneous and isotropic stress are well predicted by the smooth model (see figure).

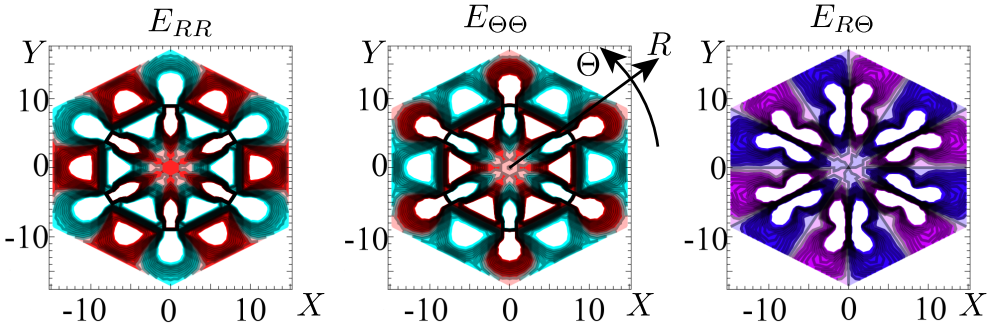

Figure S4: Map of the strain E_{RR}, $E_{\Theta\Theta}$, $E_{R\Theta}$ from the numerical simulation of the vertex model, pulled back in reference configuration (X, Y). Simulation parameters are listed in §S5. For E_{RR} and $E_{\Theta\Theta}$, the compressive stress is indicated in red, and tensile stress in blue. Out-of-range values are trimmed and shown in white. For $E_{R\Theta}$, our color code goes from blue to purple. Note that the strain is highly non-axisymmetric, with sharp singularities developing at the vertices of the hexagonal contour C. In spite of this, the analytical model based on an averaging in the Θ direction gives remarkably good results.

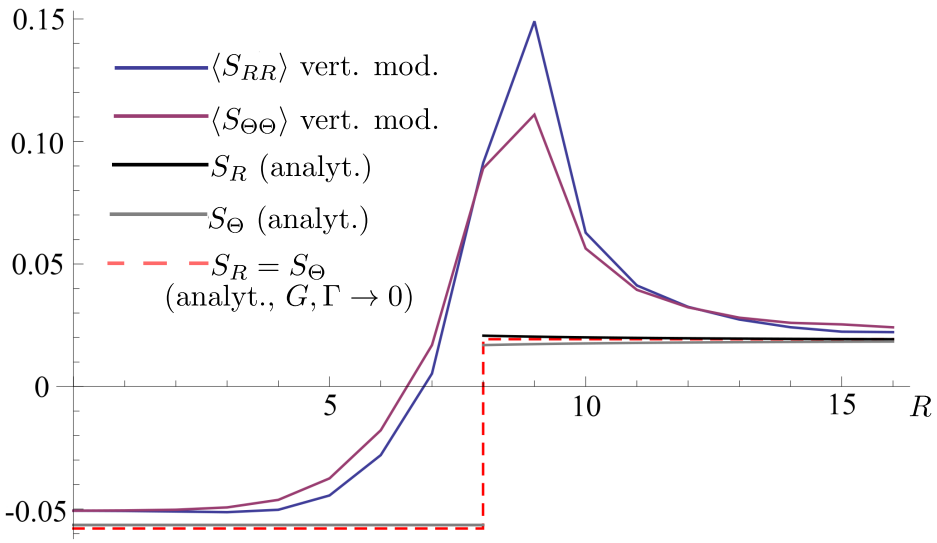

Figure S5: Comparison of the radial membrane stress $\langle S_{RR}\rangle$ and azimuthal membrane stress $\langle S_{\Theta\Theta}\rangle$ averaged over the azimuthal direction Θ from simulations of the vertex model simulation. The parameters are the same as in figure S4 and are listed in the text. This averaged stress is compared to the stress predicted by the axisymmetric plate model, both for finite G and Γ, see equation (34), and in the area-preserving limit $G, \Gamma \to 0$ in equation (36) (dashed piecewise constant curve).

S6 Mathematica code used for homogenization

Homogeneization of the vertex model for a hexagonal lattice by Fourier analysis

Basile Audoly
July 2014, last upated April 2015

Geometry and displacement

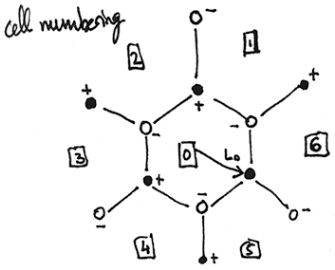

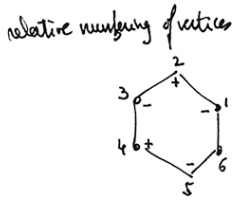

Centers of cells (central cell and adjacent ones) in reference configurations
Position of vertices in reference configuration: vertices are labelled by their relative position with respect to a cell (each vertex can be reached by the three adjacent cells)

```
cellRefCenter[cellIdx_] := Which[
    cellIdx === 0, {0, 0},
    cellIdx ≤ 6 && cellIdx > 0, (cellIdx * π/3 // {Cos[#], Sin[#]} &) L0 √3 ,
    True, Abort[]
  ];
vertexRefPos[cellIdx_, vertexIdx_] := If[
    vertexIdx > 0 && vertexIdx ≤ 6,
    L0 * (π/6 (2 vertexIdx - 1) // {Cos[#], Sin[#]} &) + cellRefCenter[cellIdx],
    Abort[]
  ];
```

```
(* check that vertex (0,1)=(5,3)=(6,5) *)
Map[Apply[vertexRefPos, #] &, {{0, 6}, {5, 2}, {6, 4}}] // Differences // Norm
```

0

```
(* graphic check *)
Graphics[Table[(Point[vertexRefPos[cellIdx, vertexIdx]] /. L0 → 1) //
    If[cellIdx == 0, {PointSize[.02], Gray, #}, {PointSize[.01], Orange, #}] &,
  {cellIdx, 0, 6}, {vertexIdx, 6}]]
```

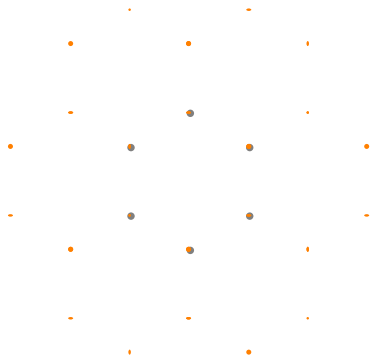

Real (r) and imaginary (i) parts of complex amplitudes for (u, v, w) (macrosopic displacement) and (p,q,s) (microscopic displacement

```
realAmplitudes = {ur, ui, vr, vi, pr, pi, qr, qi, wr, wi, sr, si}
```

{ur, ui, vr, vi, pr, pi, qr, qi, wr, wi, sr, si}

Deformed position given by x=a*X + Re((Umacro + Umicro) $e^{i\eta K.X}$), Umacro = $\begin{pmatrix}(u_r + i\,u_i)\,\eta\\(v_r + i\,v_i)\,\eta\\w_r + i\,w_i\end{pmatrix}$ and

Umicro = $\pm\frac{\eta^2}{2}\begin{pmatrix}p_r + i\,q_i\\q_r + i\,q_i\\s_r + i\,s_i\end{pmatrix}$

```
vertexDefPos[cellIdx_, vertexIdx_] := Module[{X, pm},
  X = vertexRefPos[cellIdx, vertexIdx];
  pm = (-1)^vertexIdx;
  (* alternating sign in microscopic displacement *)
  Append[a X, 0] + Re[{ (η (ur + i ui) + pm η^2 (pr + i pi)/2),
      (η (vr + i vi) + pm η^2 (qr + i qi)/2), ((wr + i wi) + pm η^2 (sr + i si)/2)} * e^(i η {kx,ky}.X)] //
   Simplify[FunctionExpand[# /. Re[a_ b_] :> Re[Expand[a b]]] // ExpToTrig,
     η ∈ Reals && kx ∈ Reals && ky ∈ Reals && L0 ∈ Reals &&
      (And @@ Map[# ∈ Reals &, realAmplitudes])] &
 ]
```

```
(* example *)
vertexDefPos[0, 6]
```

$$\left\{\frac{1}{2}\left(\sqrt{3}\ \mathrm{a}\ \mathrm{L0}+\eta\ (2\ \mathrm{ur}+\mathrm{pr}\ \eta)\ \mathrm{Cos}\left[\frac{1}{2}\left(\sqrt{3}\ \mathrm{kx}-\mathrm{ky}\right)\ \mathrm{L0}\ \eta\right]-\right.\right.$$
$$\left.\eta\ (2\ \mathrm{ui}+\mathrm{pi}\ \eta)\ \mathrm{Sin}\left[\frac{1}{2}\left(\sqrt{3}\ \mathrm{kx}-\mathrm{ky}\right)\ \mathrm{L0}\ \eta\right]\right),$$
$$\frac{1}{2}\left(-\mathrm{a}\ \mathrm{L0}+\eta\ (2\ \mathrm{vr}+\mathrm{qr}\ \eta)\ \mathrm{Cos}\left[\frac{1}{2}\left(\sqrt{3}\ \mathrm{kx}-\mathrm{ky}\right)\ \mathrm{L0}\ \eta\right]-\right.$$
$$\left.\eta\ (2\ \mathrm{vi}+\mathrm{qi}\ \eta)\ \mathrm{Sin}\left[\frac{1}{2}\left(\sqrt{3}\ \mathrm{kx}-\mathrm{ky}\right)\ \mathrm{L0}\ \eta\right]\right),$$
$$\left.\frac{1}{2}\left((2\ \mathrm{wr}+\mathrm{sr}\ \eta^2)\ \mathrm{Cos}\left[\frac{1}{2}\left(\sqrt{3}\ \mathrm{kx}-\mathrm{ky}\right)\ \mathrm{L0}\ \eta\right]-(2\ \mathrm{wi}+\mathrm{si}\ \eta^2)\ \mathrm{Sin}\left[\frac{1}{2}\left(\sqrt{3}\ \mathrm{kx}-\mathrm{ky}\right)\ \mathrm{L0}\ \eta\right]\right)\right\}$$

```
(* check that vertex (0,1)=(5,3)=(6,5) match in deformed configuration *)
Map[Apply[vertexDefPos, #] &, {{0, 6}, {5, 2}, {6, 4}}] // Differences // Norm
```

```
0
```

Definition of area vector A_k

```
AkVector[cellIdx_] :=
 Table[vertexDefPos[cellIdx, vertexIdx], {vertexIdx, 6}] // Append[
          #, First[#]] & // {Most[#], Rest[#]} & // Transpose //
     Map[1/2 #[[1]] × #[[2]] &, #] & // Total // Series[#, {η, 0, 4}] & // Simplify
```

L0 such that reference area is A0=1, based on the formula for the area of an hexagon

```
L0Rule = {L0 → Sqrt[2/(3 Sqrt[3])]};
```

Compute area vector, scalar area and unit normal for the central and 6 peripheral cells

```
ProcessSevenCells = Table[
   Module[{akv, aks, nk},
    Print["Processing cell #", cellIdx, "..."];
    akv = AkVector[cellIdx];
    aks = akv // Norm // # /. Abs[u_]^2 :> u^2 & // Simplify[#, a > 0 && L0 > 0] &;
    nk = akv/aks // Simplify[# /. L0Rule] &;
    <|"vector" → akv, "scalar" → aks, "normal" → nk|>
   ],
   {cellIdx, 0, 6}];
processedCentralCell = ProcessSevenCells[[1]];
processedPeriphCells = ProcessSevenCells[[2 ;; -1]];
```

```
Processing cell #0...
Processing cell #1...
Processing cell #2...
Processing cell #3...
Processing cell #4...
Processing cell #5...
Processing cell #6...
```

Energy terms

Terms involving area

```
areaTerm =
 processedCentralCell // 1/2 (#[["scalar"]] - 1)^2 & // Simplify[# /. L0Rule, a > 0] &
```

$$\frac{1}{2}\left(-1+a^2\right)^2-\frac{1}{2}\left(\left(-1+a^2\right)\left(2\,a\left(kx\,ui+ky\,vi\right)-\left(kx^2+ky^2\right)wi^2\right)\right)\eta^2+$$
$$\frac{1}{8}\left(\left(-2\,a\left(kx\,ui+ky\,vi\right)+\left(kx^2+ky^2\right)wi^2\right)^2+\right.$$
$$\frac{1}{9\,a^2}\left(-1+a^2\right)\left(3^{1/4}\,a^3\left(2\times 3^{1/4}\,kx^3\,ui+2\,kx\,ky\left(3\sqrt{2}\,pr+3^{1/4}\,ky\,ui\right)+ky^2\left(-3\sqrt{2}\,qr+\right.\right.\right.$$
$$\left.\left.\left.2\times 3^{1/4}\,ky\,vi\right)+kx^2\left(3\sqrt{2}\,qr+2\times 3^{1/4}\,ky\,vi\right)\right)-2\sqrt{3}\,a^2\left(kx^2+ky^2\right)^2wi^2+\right.$$
$$\left.36\,a\left(kx^2+ky^2\right)\left(kx\,ui+ky\,vi\right)wi^2-9\left(kx^2+ky^2\right)^2wi^4\right)\Big)\eta^4+O[\eta]^5$$

```
normalsDotTerm = Map[1 - (processedCentralCell[["normal"]]).(#[["normal"]]) &,
    processedPeriphCells] // Simplify //
  (*the coefficient 2 is because each edge is counted twice
   (one for each adjacent face) *) B/2 * Total[#] & // Simplify[# /. L0Rule] &
```

$$\frac{\sqrt{3}\,B\left(kx^2+ky^2\right)^2wr^2\,\eta^4}{2\,a^2}+O[\eta]^5$$

Terms involving segment lengths

```
meanEdgeLength =
 Map[Norm, Table[vertexDefPos[0, vertexIdx], {vertexIdx, 6}] // Append[
     #, First[#]] & // Differences] // # /. Abs → Identity & //
   Series[#, {η, 0, 4}] & // Mean // Simplify[# /. L0Rule, a > 0] &
```

$$\frac{\sqrt{2}\,a}{3^{3/4}}+\frac{\left(-2\,a\left(kx\,ui+ky\,vi\right)+\left(kx^2+ky^2\right)wi^2\right)\eta^2}{2\sqrt{2}\,3^{3/4}\,a}+$$
$$\frac{1}{288\sqrt{2}\,3^{1/4}\,a^3}\left(4\,a^3\left(2\,kx^3\,ui+2\,kx\,ky\left(\sqrt{2}\,3^{3/4}\,pr+ky\,ui\right)+\right.\right.$$
$$ky^2\left(-\sqrt{2}\,3^{3/4}\,qr+2\,ky\,vi\right)+kx^2\left(\sqrt{2}\,3^{3/4}\,qr+2\,ky\,vi\right)\Big)+$$
$$36\times 3^{1/4}\,a\left(3^{1/4}\,kx^3\,ui+kx\,ky\left(-2\sqrt{2}\,pr+3^{1/4}\,ky\,ui\right)+kx^2\left(-\sqrt{2}\,qr+3^{1/4}\,ky\,vi\right)+\right.$$
$$\left.ky^2\left(\sqrt{2}\,qr+3^{1/4}\,ky\,vi\right)\right)wi^2-9\sqrt{3}\left(kx^2+ky^2\right)^2wi^4+$$
$$2\,a^2\left(108\,pr^2+108\,qr^2+216\,sr^2+6\sqrt{3}\,kx^2\,ui^2+18\sqrt{3}\,ky^2\,ui^2-\right.$$
$$24\sqrt{3}\,kx\,ky\,ui\,vi+18\sqrt{3}\,kx^2\,vi^2+6\sqrt{3}\,ky^2\,vi^2+$$
$$36\sqrt{2}\,3^{1/4}\,pr\left(ky\,ui+kx\,vi\right)+36\sqrt{2}\,3^{1/4}\,qr\left(kx\,ui-ky\,vi\right)-4\,kx^4\,wi^2-$$
$$\left.\left.8\,kx^2\,ky^2\,wi^2-4\,ky^4\,wi^2+3\,kx^4\,wr^2+6\,kx^2\,ky^2\,wr^2+3\,ky^4\,wr^2\right)\right)\eta^4+O[\eta]^5$$

```
{lineTensionTerm, perimeterTerm} =
  {G * 6/2 * meanEdgeLength, H/2 * (6 meanEdgeLength)^2} // Simplify;
```

Assembling

```
allTerms = areaTerm + lineTensionTerm + perimeterTerm + normalsDotTerm // Simplify
```

$$\left(\frac{1}{2}\left(-1+a^2\right)^2+\sqrt{2}\ 3^{1/4}\ a\ G+4\ \sqrt{3}\ a^2\ H\right)-\frac{\left(\left(2\ a^3+\sqrt{2}\ 3^{1/4}\ G+a\left(-2+8\ \sqrt{3}\ H\right)\right)\ \left(2\ a\ \left(kx\ ui+ky\ vi\right)-\left(kx^2+ky^2\right)\ wi^2\right)\right)\ \eta^2}{4\ a}+$$

$$\frac{1}{576}\left(72\ \left(\left(-2\ a\ \left(kx\ ui+ky\ vi\right)+\left(kx^2+ky^2\right)\ wi^2\right)^2+\frac{1}{9\ a^2}\left(-1+a^2\right)\ \left(3^{1/4}\ a^3\ \left(2\times 3^{1/4}\ kx^3\ ui+2\ kx\ ky\ \left(3\ \sqrt{2}\ pr+3^{1/4}\ ky\ ui\right)+ky^2\ \left(-3\ \sqrt{2}\ qr+2\times 3^{1/4}\ ky\ vi\right)+kx^2\ \left(3\ \sqrt{2}\ qr+2\times 3^{1/4}\ ky\ vi\right)\right)-2\ \sqrt{3}\ a^2\ \left(kx^2+ky^2\right)^2\ wi^2+36\ a\ \left(kx^2+ky^2\right)\ \left(kx\ ui+ky\ vi\right)\ wi^2-9\ \left(kx^2+ky^2\right)^2\ wi^4\right)\right)+\frac{288\ \sqrt{3}\ B\ \left(kx^2+ky^2\right)^2\ wr^2}{a^2}+\frac{1}{a^3}\sqrt{2}\ 3^{3/4}\ G\ \left(4\ a^3\ \left(2\ kx^3\ ui+2\ kx\ ky\ \left(\sqrt{2}\ 3^{3/4}\ pr+ky\ ui\right)+ky^2\ \left(-\sqrt{2}\ 3^{3/4}\ qr+2\ ky\ vi\right)+kx^2\ \left(\sqrt{2}\ 3^{3/4}\ qr+2\ ky\ vi\right)\right)+36\times 3^{1/4}\ a\ \left(3^{1/4}\ kx^3\ ui+kx\ ky\ \left(-2\ \sqrt{2}\ pr+3^{1/4}\ ky\ ui\right)+kx^2\ \left(-\sqrt{2}\ qr+3^{1/4}\ ky\ vi\right)+ky^2\ \left(\sqrt{2}\ qr+3^{1/4}\ ky\ vi\right)\right)\ wi^2-9\ \sqrt{3}\ \left(kx^2+ky^2\right)^2\ wi^4+2\ a^2\ \left(108\ pr^2+108\ qr^2+216\ sr^2+6\ \sqrt{3}\ kx^2\ ui^2+18\ \sqrt{3}\ ky^2\ ui^2-24\ \sqrt{3}\ kx\ ky\ ui\ vi+18\ \sqrt{3}\ kx^2\ vi^2+6\ \sqrt{3}\ ky^2\ vi^2+36\ \sqrt{2}\ 3^{1/4}\ pr\ \left(ky\ ui+kx\ vi\right)+36\ \sqrt{2}\ 3^{1/4}\ qr\ \left(kx\ ui-ky\ vi\right)-4\ kx^4\ wi^2-8\ kx^2\ ky^2\ wi^2-4\ ky^4\ wi^2+3\ kx^4\ wr^2+6\ kx^2\ ky^2\ wr^2+3\ ky^4\ wr^2\right)\right)+\frac{1}{a^2}24\ H\ \left(4\ a^3\ \left(2\ kx^3\ ui+2\ kx\ ky\ \left(\sqrt{2}\ 3^{3/4}\ pr+ky\ ui\right)+ky^2\ \left(-\sqrt{2}\ 3^{3/4}\ qr+2\ ky\ vi\right)+kx^2\ \left(\sqrt{2}\ 3^{3/4}\ qr+2\ ky\ vi\right)\right)+12\times 3^{1/4}\ a\ \left(3^{1/4}\ kx^3\ ui+kx\ ky\ \left(-6\ \sqrt{2}\ pr+3^{1/4}\ ky\ ui\right)+kx^2\ \left(-3\ \sqrt{2}\ qr+3^{1/4}\ ky\ vi\right)+ky^2\ \left(3\ \sqrt{2}\ qr+3^{1/4}\ ky\ vi\right)\right)\ wi^2-3\ \sqrt{3}\ \left(kx^2+ky^2\right)^2\ wi^4+2\ a^2\ \left(108\ pr^2+108\ qr^2+216\ sr^2+18\ \sqrt{3}\ kx^2\ ui^2+18\ \sqrt{3}\ ky^2\ ui^2+18\ \sqrt{3}\ kx^2\ vi^2+18\ \sqrt{3}\ ky^2\ vi^2+36\ \sqrt{2}\ 3^{1/4}\ pr\ \left(ky\ ui+kx\ vi\right)+36\ \sqrt{2}\ 3^{1/4}\ qr\ \left(kx\ ui-ky\ vi\right)-4\ kx^4\ wi^2-8\ kx^2\ ky^2\ wi^2-4\ ky^4\ wi^2+3\ kx^4\ wr^2+6\ kx^2\ ky^2\ wr^2+3\ ky^4\ wr^2\right)\right)\right)\ \eta^4+O[\eta]^5$$

Define energy for homogeneous transformations

```
w = allTerms // Normal // # /. η → 0 & // Function @@ {a, #} &
```

$$\text{Function}\left[a,\ \frac{1}{2}\left(-1+a^2\right)^2+\sqrt{2}\ 3^{1/4}\ a\ G+4\ \sqrt{3}\ a^2\ H\right]$$

Equation for a definition confirguration PE (planar equilibrium)

```
-w'[a]/(2 a) // Simplify
```

$$1 - a^2 - \frac{3^{1/4}\, G}{\sqrt{2}\, a} - 4\sqrt{3}\, H$$

Let us define $\tilde{G}$ which incoporates some numerical factors into G for convenience

```
Needs["Notation`"];
Symbolize[ G̃ ];
toGt = {G → a √2 G̃ / 3^(1/4)};
-w'[a]/(2 a) /. toGt // Simplify
```

$$1 - a^2 - \tilde{G} - 4\sqrt{3}\, H$$

```
(* spin-like matrices *)
Sx = {{0, 1}, {1, 0}};
Sy = {{1, 0}, {0, -1}};
S = {Sx, Sy};
SDoubleContract[t_] := TensorContract[S⊗t, {{2, 4}, {3, 5}}];
```

We simplified the total energy manually and came up with the expression below, which we check for correctness (notice that result is zero)

```
KdotVim = kx ui + ky vi;
KSq = kx^2 + ky^2;
KVec = {kx, ky};
QreVec = {pr, qr};
VimVec = {ui, vi};
allTerms - (
    w[a] + w'[a]/(2 a) (- a KdotVim + 1/2 KSq wi^2) η^2 +
     + (w'[a]/(24 √3) (KSq KdotVim - KSq^2/a wi^2 + 3^(3/4)/√2 QreVec.SDoubleContractionProduct[KVec⊗KVec]) +
          (2 a^2 - G̃)/4 KdotVim^2
          + (1/4 G̃ + √3 H) (3/2 KSq VimVec.VimVec + 3 √3 (QreVec.QreVec + 2 sr^2) +
               √2 3^(3/4) QreVec.SDoubleContractionProduct[KVec⊗(VimVec - 1/(2 a) wi^2 KVec)]) +
          1/(8 a^2) (1 - 3/4 G̃ - √3 H) (-4 a KSq KdotVim wi^2 + KSq^2 wi^4) +
          1/(4 √3) (G̃/4 + √3 H + 6 B/a^2) KSq^2 wr^2
        ) η^4
    ) // Simplify[# /. toGt] &
O[η]^5
```

Cauchy-Green strain

Deformation gradient

```
Fsmooth = a {X, Y, 0} + Re[{η (ur + i ui), η (vr + i vi), (wr + i wi)} * e^(i η {kx,ky}.{X,Y})] //
        ExpToTrig // # /. Re[a_ b_] :> Re[Expand[a b]] & //
      Simplify[#, kx ∈ Reals && ky ∈ Reals && η ∈ Reals && X ∈ Reals &&
          Y ∈ Reals && (And @@ Map[# ∈ Reals &, realAmplitudes])] & //
     {D[#, X], D[#, Y]} & // Transpose;
Fsmooth // MatrixForm
```

$$\begin{pmatrix} a - kx\,ui\,\eta^2 \cos[kx\,X\,\eta + ky\,Y\,\eta] - kx\,ur\,\eta^2 \sin[kx\,X\,\eta + ky\,Y\,\eta] & -ky\,ui\,\eta^2 \cos[kx\,X\,\eta + ky\,Y\,\eta] \\ -kx\,vi\,\eta^2 \cos[kx\,X\,\eta + ky\,Y\,\eta] - kx\,vr\,\eta^2 \sin[kx\,X\,\eta + ky\,Y\,\eta] & a - ky\,vi\,\eta^2 \cos[kx\,X\,\eta + ky\,Y\,\eta] \\ -kx\,wi\,\eta \cos[kx\,X\,\eta + ky\,Y\,\eta] - kx\,wr\,\eta \sin[kx\,X\,\eta + ky\,Y\,\eta] & -ky\,wi\,\eta \cos[kx\,X\,\eta + ky\,Y\,\eta] \end{pmatrix}$$

Cauchy - Green strain at origin

```
Eo = Transpose[Fsmooth].Fsmooth //
   Simplify[(# - a^2 IdentityMatrix[2])/(2 a) /. {X → 0, Y → 0}] &
```

$$\left\{\left\{\frac{kx\,\eta^2\left(-2\,a\,ui+kx\left(wi^2+\left(ui^2+vi^2\right)\eta^2\right)\right)}{2\,a},\ \frac{\eta^2\left(-a\left(ky\,ui+kx\,vi\right)+kx\,ky\left(wi^2+\left(ui^2+vi^2\right)\eta^2\right)\right)}{2\,a}\right\},\ \left\{\frac{\eta^2\left(-a\left(ky\,ui+kx\,vi\right)+kx\,ky\left(wi^2+\left(ui^2+vi^2\right)\eta^2\right)\right)}{2\,a},\ \frac{ky\,\eta^2\left(-2\,a\,vi+ky\left(wi^2+\left(ui^2+vi^2\right)\eta^2\right)\right)}{2\,a}\right\}\right\}$$

Check of formula for E(0, 0) proposed in SI

```
-η^2 {ui, vi}⊗{kx, ky} + η^2/(2 a) {kx, ky}⊗{kx, ky} (η^2 (ui^2 + vi^2) + wi^2) //
   (# + Transpose[#])/2 & // Simplify[Eo - #] &
```

$$\{\{0, 0\}, \{0, 0\}\}$$

Identification of expansion at order 2

Cancellation of the η^2 term in the energy follows from the condition w'(a)=0 used earlier

```
allTerms - (w'[a]/2 Tr[Eo]) // Normal // CoefficientList[#, η] & // #[[3]] & //
   # /. toGt & // Simplify
```

$$0$$

Identification of expansion at order 4

```
elimG = Solve[w'[a] == 0, G] // First
```

$$\left\{G \to -\frac{\sqrt{2}\left(-a+a^3+4\sqrt{3}\,a\,H\right)}{3^{1/4}}\right\}$$

```
(* now  G̃ as a function of a *)
Solve[(G /. elimG) == (G /. toGt), G̃]
```

$$\left\{\left\{\tilde{G} \to 1-a^2-4\sqrt{3}\,H\right\}\right\}$$

```
coefsDirectMethod =
  allTerms - (w[a] + 1/2 λStar Tr[Eo]^2 + μStar Tr[Eo.Eo] + β/2 η^4 (kx^2 + ky^2)^2 wr^2 +
                τ/2 η^4 (pr^2 + qr^2 + 2 sr^2) - γ η^2 {pr, qr}.SDoubleContract[Eo]) //
           Expand[# /. elimG] & // CoefficientList[#, {kx, ky, ui, vi, wi,
             wr, pr, qr, sr}] & // Flatten // Union // Map[# == 0 &, #] & //
     Simplify // Solve[#, {λStar, μStar, β, τ, γ}] & // Simplify
```

$$\left\{\left\{\lambda\text{Star} \to \frac{1}{4}\left(-5+9\,a^2+8\sqrt{3}\,H\right),\ \mu\text{Star} \to -\frac{3}{4}\left(-1+a^2\right),\right.\right.$$
$$\left.\left.\beta \to \frac{a^2-a^4+24\,B}{8\sqrt{3}\,a^2},\ \tau \to -\frac{3}{2}\sqrt{3}\left(-1+a^2\right),\ \gamma \to -\frac{3^{3/4}\left(-1+a^2\right)}{2\sqrt{2}}\right\}\right\}$$

Relaxing the microscopic displacement δ

Check formulas calculated by hand for optimum of energy with respect to {δxr, δyr}

```
CauchyGreenFormal = Array[CGf, {2, 2}] /. CGf[1, 2] → CGf[2, 1]
 (* a symmetric matrix *);
```

A useful identity

```
(SDoubleContract[CauchyGreenFormal] // #.# &) -
   (- Tr[CauchyGreenFormal]^2 + 2 Tr[CauchyGreenFormal.CauchyGreenFormal]) //
 (*Solve[#==0,{α,β}]&//*)Simplify
```

```
0
```

```
microEnergy = τ/2 (pr^2 + qr^2) - γ Tr[CauchyGreenFormal.S.{pr, qr}];
(* as found above by identification *)
microOptimum = {{pr, qr}, γ/τ SDoubleContract[CauchyGreenFormal]} // Transpose //
   Map[Rule @@ # &, #] &;
(* check that this value of δ is the optimum *)
Table[D[microEnergy, δ], {δ, {pr, qr}}] /. microOptimum // Simplify
```

```
{0, 0}
```

Optimum value of the energy

```
(microEnergy /. microOptimum) -
   (-γ^2/(2 τ) (SDoubleContract[CauchyGreenFormal] // #.# &)) // Simplify
```

```
0
```

Same quantity, rewritten in terms of invariants

```
(microEnergy /. microOptimum) -
   (-γ^2/(2 τ) (-Tr[CauchyGreenFormal]^2 + 2 Tr[CauchyGreenFormal.CauchyGreenFormal])) //
 Simplify
```

```
0
```

```
γ^2/τ /. coefsDirectMethod(* numerical value of the coefficient —
  mind the factor 1/2, which has been left out *)
```

$$\left\{\frac{1}{4}\left(1-a^2\right)\right\}$$

```
renormalizedCoefs =
 1/2 λ Tr[CauchyGreenFormal]^2 + μ Tr[CauchyGreenFormal.CauchyGreenFormal] - γ^2/(2 τ)
      (-Tr[CauchyGreenFormal]^2 + 2 Tr[CauchyGreenFormal.CauchyGreenFormal]) // <|
     λrenorm → 2 * Coefficient[#, Tr[CauchyGreenFormal]^2], μrenorm →
      Coefficient[#, Tr[CauchyGreenFormal.CauchyGreenFormal]]|> & // Expand
```

$$\left\langle\left|\lambda\text{renorm}\to 2\left(\frac{\lambda}{2}+\frac{\gamma^2}{2\,\tau}\right),\ \mu\text{renorm}\to\mu-\frac{\gamma^2}{\tau}\right|\right\rangle$$

```
renormalizedCoefsFinal = renormalizedCoefs /. coefsDirectMethod // Simplify
```

$$\left\{\left\langle\left|\lambda\text{renorm}\to 2\left(\frac{1}{8}\left(1-\text{a}^2\right)+\frac{1}{8}\left(-5+9\,\text{a}^2+8\sqrt{3}\,\text{H}\right)\right),\ \mu\text{renorm}\to\frac{1}{2}\left(1-\text{a}^2\right)\right|\right\rangle\right\}$$

Linearized moduli (a is close to 1, and H and B are small)

Listed in main text, equation 9

```
{G /. elimG,
      λrenorm /. renormalizedCoefsFinal,
      μrenorm /. renormalizedCoefsFinal,
      β /. coefsDirectMethod,
      λrenorm / (2 μrenorm + λrenorm) (* Poisson's coef *) /. renormalizedCoefsFinal} /.
    {a → 1 - η OneMinusA, H → η HH, B → η BB} //
   Flatten // Series[#, {η, 0, 1}] & // Normal
```

$$\left\{\left(-4\sqrt{2}\,3^{1/4}\,\text{HH}+\frac{2\sqrt{2}\,\text{OneMinusA}}{3^{1/4}}\right)\eta,\ 1+\left(2\sqrt{3}\,\text{HH}-4\,\text{OneMinusA}\right)\eta,\right.$$
$$\left.\text{OneMinusA}\,\eta,\ \left(\sqrt{3}\,\text{BB}+\frac{\text{OneMinusA}}{4\sqrt{3}}\right)\eta,\ 1-2\,\text{OneMinusA}\,\eta\right\}$$

References

[1] M. Arroyo and T. Belytschko. An atomistic-based finite deformation membrane for single-layer crystalline films. *Journal of the Mechanics and Physics of Solids*, 50:1941—1977, 2002.

[2] M. Arroyo and T. Belytschko. Finite crystal elasticity of carbon nanotubes based on the exponential cauchy-born rule. *Physical Review B (Condensed Matter and Materials Physics)*, 69:115415, 2004.

[3] B. Audoly and Y. Pomeau. Elasticity and geometry. In R. Kaiser and J. Montaldi, editors, *Peyresq Lecture Notes on Nonlinear Phenomena*, chapter 1, pages 1–35. World Scientific, 2000.

[4] C. S. G. Cousins. Inner elasticity. *Journal of Physics C: Solid State Physics*, 11:4867–4879, 1978.

[5] J. W. Hutchinson and Z. Suo. Mixed mode cracking in layered materials. *Advances in Applied Mechanics*, 29:63–191, 1992.

[6] D.B. Staple, R. Farhadifar, J.-C. Röper, B. Aigouy, S. Eaton, and F. Jülicher. Mechanics and remodelling of cell packings in epithelia. *The European Physical Journal E*, 33(2):117–127, 2010.

[7] S. Timoshenko and J. M. Gere. *Theory of elastic stability*. MacGraw Hill, New York, 2$^{\text{nd}}$ edition, 1961.

[8] Wolfram Research, Inc. Mathematica edition: Version 10.0. Champaign, IL (USA), 2014.

[9] J. Wu, K. C. Hwang, and Y. Huang. An atomistic-based finite-deformation shell theory for single-wall carbon nanotubes. *Journal of the Mechanics and Physics of Solids*, 56(1):279–292, 2008.